Palaeogeography, Palaeoclimatology, Palaeoecology 681 (2026) 113377

Contents lists available at ScienceDirect

Palaeogeography, Palaeoclimatology, Palaeoecology

journal homepage: www.elsevier.com/locate/palaeo

Astronomical climate forcing and tuning of the Baringo core (HSPDP-BTB13-1A), Kenya

Bianca R. Spiering[a,*], Mark J. Sier[a,b], Frederik J. Hilgen[a]

[a] Department of Earth Sciences, Faculty of Geosciences, Utrecht University, Utrecht, 3584 CB, the Netherlands
[b] CENIEH, Paseo Sierra de Atapuerca 3, 09002, Burgos, Spain

ARTICLE INFO

Editor: Professor L Angiolini

Keywords:
Chemeron Formation
Pliocene-Pleistocene
Astronomical tuning
Paleoclimate
East African Rift
Obliquity

ABSTRACT

The core from the Baringo-Tugen Hills-Barsemoi paleolake area in Kenya (called BTB13) provides an excellent opportunity to study east African hydroclimate in relation to human evolution and global climate change during the Pliocene-Pleistocene transition. As age control is critical, a Bayesian age model was previously constructed based on magnetostratigraphy and radio-isotopic dating. In order to improve the existing age model, we astronomically-tune the BTB13 core using the available gamma density (GD) and magnetic susceptibility (MS) records. Spectral analysis and bandpass filtering revealed a dominance of obliquity-related variability, which was used to establish an initial tuning. Significant precession-related variability was subsequently used to tune the records to precession and a standardized obliquity-precession target curve. The precession-paced variability is in very good agreement with precession-obliquity interference, making a shift in the tuning unlikely. Deep lake phases, characterized by diatomites and MS and GD minima, were related to precession minima and obliquity maxima, indicating a link to the intensification of the North African monsoon in response to boreal summer insolation maxima. This is further supported by the simultaneous formation of diatomites with Mediterranean sapropels. The obliquity dominance might be explained by a combination of the cross-equatorial insolation gradient and the seasonal cycle of equatorial insolation, and/or a link to higher latitudes.

1. Introduction

The East African Rift Valley contains a rich record of paleoanthropological and archaeological sites as well as similarly-aged paleolakes in which east African climate changes were recorded (Campisano et al., 2017). In order to investigate the relationship between human evolution and climate change, cores were retrieved of several of these paleolake stratigraphies by the Hominin Sites and Paleolakes Drilling Project (HSPDP; Cohen et al., 2016). Within the East African Rift Valley, the central Kenya Rift contains the most complete Neogene succession known to date (Chapman and Brook, 1978). Here, the Pliocene-Pleistocene-aged Chemeron Formation was drilled, which, in outcrop, contains three hominin sites and many other fossil vertebrate localities (Cohen et al., 2016). This core provides a relatively long and continuous terrestrial record of eastern African hydroclimate for a time interval with major climatic transitions, namely the onset of global cooling and northern hemisphere glaciation (Raymo, 1994), as well as important hominin events, such as early stone tools (Harmand et al., 2015), extinction of *Australopithecus afarensis* (Lockwood et al., 2000), and first appearance of *Homo* (Villmoare et al., 2015; see Potts and Faith, 2015 for an overview).

A precise chronological framework is crucial to place these events in a regional context. A Bayesian age model was generated for the cored Chemeron Formation based on magnetostratigraphy and $^{40}Ar/^{39}Ar$ dating of tuffs in the core and outcrop (Deino et al., 2021). The model includes 30 control points and is relatively precise with a 95 % confidence interval of ~120 kyr or less (Deino et al., 2021). Application of the age model on the available proxy data of the core revealed the influence astronomical climate forcing, particularly precession and obliquity (Mitsunaga et al., 2023; Sier et al., 2025; see Supplementary Materials for general theoretical background). The influence of precession was also previously recognized in an outcrop interval correlative to the top part of the core, which consists of five recurring diatomites (Deino et al., 2006; Kingston et al., 2007). Despite the inferred presence of astronomical cyclicity, no attempt was yet made to develop an astronomical tuning and thereby improve the accuracy, precision and resolution of the existing age model.

In this study, we present a cyclostratigraphic analysis and

* Corresponding author.
E-mail addresses: b.r.spiering@uu.nl (B.R. Spiering), F.J.Hilgen@uu.nl (F.J. Hilgen).

https://doi.org/10.1016/j.palaeo.2025.113377
Received 30 April 2025; Received in revised form 14 October 2025; Accepted 25 October 2025
Available online 28 October 2025

astronomical tuning of the cored Chemeron Formation from the Kenya Rift. Our analyses were based on the available magnetic susceptibility and gamma density data of the core (Cohen et al., 2016). We first performed spectral analysis on the data in the depth domain and time domain using the Bayesian age model of Deino et al. (2021). Subsequently, these results were used to correlate the data to the astronomical solution, after which spectral analysis was performed again on the astronomically-tuned data. The analysis and tuning of the astronomical controlled cyclicity in the cored Chemeron Formation contributes to an improved understanding of eastern African climate change and provides a precise chronological framework against which other regional or global climate records and hominin events can be placed.

2. Materials and methods

2.1. Materials

The 228-m-long Baringo-Tugen Hills-Barsemoi 2013 drillcore (HSPDP-BTB13-1A; hereafter referred to as BTB13) was obtained as part of the Hominin Sites and Paleolakes Drilling Project (HSPDP; Cohen et al., 2016). The drill site is located in the Baringo Basin in Kenya, in between the Tugen Hills and Lake Baringo (0.5546°N, 35.9375°E). The Baringo Basin is located in the central Kenya Rift, which is part of the East African Rift System. The core consists of fluvio-lacustrine sedimentary rocks and tuffs of the Pliocene-Pleistocene-aged Chemeron Formation (5.3 to 1.6 Ma; Chapman and Brook, 1978; Deino et al., 2006), which is exposed in close proximity to the drill site. The core mainly consists of claystones, siltstones, and sandstones with some conglomerates, which are abundant in the basal and mid-upper part of the core (~228–201 and ~ 107–78 m below surface; mbs), and diatomites, which are abundant in the upper part of the core (~78–5 mbs; Deino et al., 2021). Magnetic susceptibility (MS) and gamma density (GD) were measured on the core at 0.5 cm intervals (Cohen et al., 2016; data available at Open Science Framework, https://doi.org/10.17605/OSF.IO/ANFYW).

2.2. Existing age control

A Bayesian age model was constructed based on four types of age control with a total of 30 control points: $^{40}Ar/^{39}Ar$ dating of 12 tuffs from the core, $^{40}Ar/^{39}Ar$ dating of 4 tuffs correlated to the core from outcrops, correlation of the bottom and top of 5 distinctive diatomites, which were age calibrated to outcrop $^{40}Ar/^{39}Ar$ dating and paleomagnetism (Deino et al., 2006; Kingston et al., 2007), and 4 paleomagnetic reversals in the core (Sier et al., 2021; Deino et al., 2021; Fig. 2A). The age model indicated that the core spans 730 kyr, from ~3.29 to ~2.56 Ma (Deino et al., 2021). Reconstructed sedimentation rates vary from ~39 cm/kyr and ~23 cm/kyr in the lower-middle part of the core (~230–125 mbs and ~ 125–100 mbs, respectively), decreasing to ~13 cm/kyr in the middle part of the core (~100–75 mbs), followed by an increase to 45 cm/kyr in the upper part of the core (~75–0 mbs; Deino et al., 2021). Unconformities were recognized at ~10, ~85, and ~105 mbs (Deino et al., 2021). An alternative sedimentation rate model was explored in which ~40 kyr is missing at ~105 mbs, but this was not included in the reference model (Deino et al., 2021).

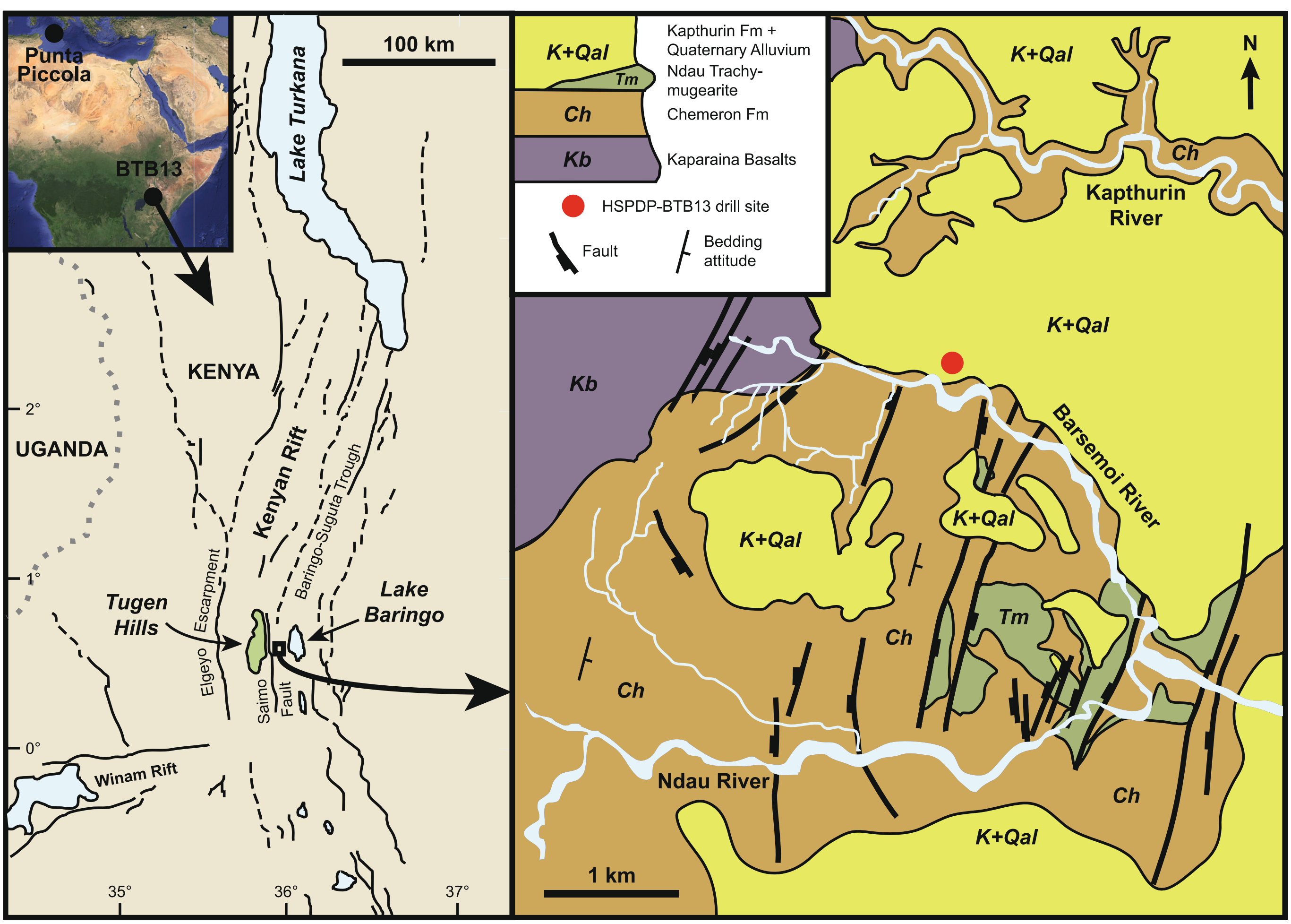

Fig. 1. Map of the BTB13 drill site in the Kenya Rift. Adapted from Deino et al. (2006).

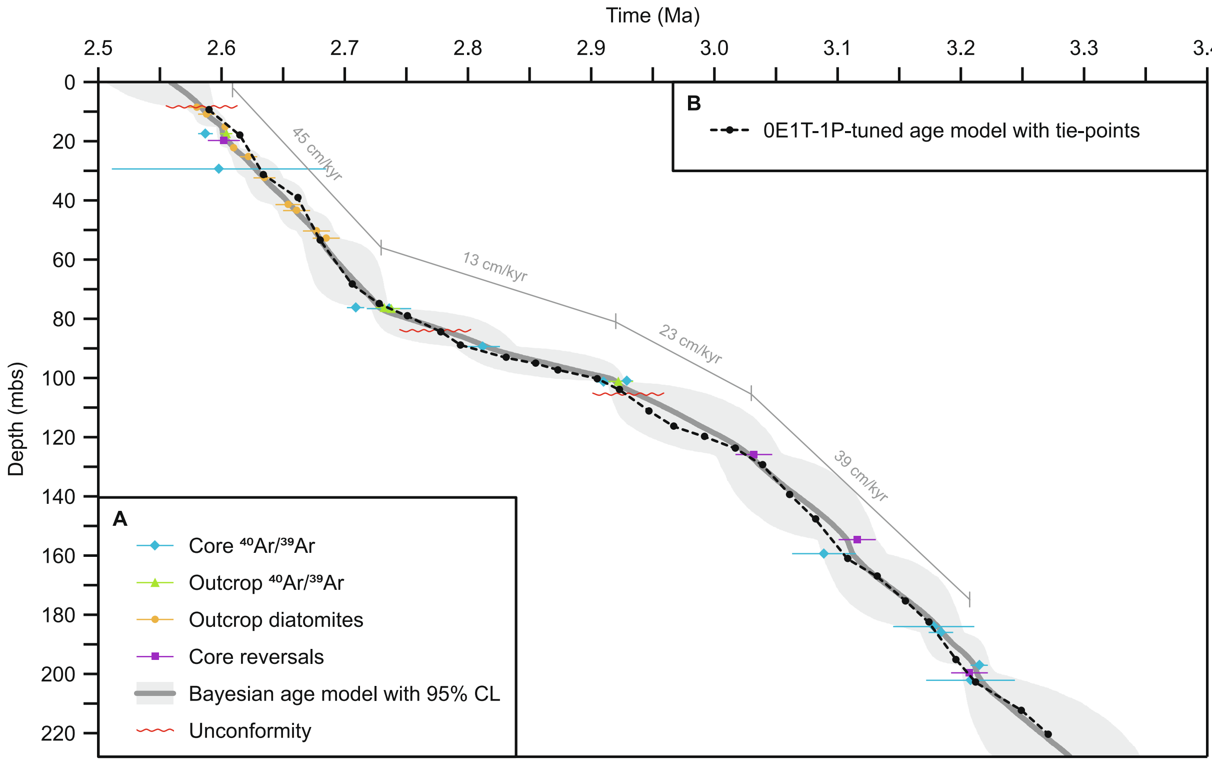

Fig. 2. Bayesian age model of the BTB13 core with 1-sigma uncertainties for age control points (Deino et al., 2021; A). Astronomically-tuned age model (this study; B).

2.3. Spectral analysis

Spectral analysis was performed with the program Acycle (version 2.8; Li et al., 2019). Although the data was analyzed in both the depth and time domain, we focused on the time domain due to the significant changes in sedimentation rate evident from the Bayesian age model (Fig. 2A). Beforehand, the data was sorted, interpolated to uniform spacing based on the median spacing, and demeaned. Power spectra were generated with the multitaper method (time-bandwidth product = 2, pad factor = 5; Thomson, 1982) and first-order autoregressive (AR1) noise confidence levels (CLs; Husson, 2014; 'Classic AR1' in Acycle). Bandpass filtering was applied using the Gauss algorithm (Kodama and Hinnov, 2015). In addition, evolutionary spectral analysis was applied on the depth series using default settings. Coherence and phase analysis was applied using default settings in Acycle to determine the phase relationship between two series for a certain periodicity. Tuning of the data was done using linear interpolation between tie-points and extrapolation at the ends of the data. The La2004 astronomical solution was used (Laskar et al., 2004).

3. Results

3.1. Depth domain

The GD and MS data display significant variability at scales of ~10–20 m (Fig. 3). The MS data varies at the ~10–20-m scale throughout the core, while the GD data shows the greatest variability at this scale between 0 and 140 mbs. Between 140 and 230 mbs, GD data is characterized by smaller-scale variability with a lower amplitude. At the ~10–20-m scale, minima in the GD data concur with minima in the MS data. Five diatomites are present in the upper 60 m (D1-D5) and one diatomite is present at ~130 mbs (D0; Deino et al., 2021). Additionally, two diatom-rich intervals are present at ~90 and ~115 mbs (DIs; Westover et al., 2021). All the diatomites and diatom-rich intervals concur with GD and MS minima (Fig. 3).

Spectral analysis shows that the GD and MS data are dominated by significant (>95 % CL) spectral power at periodicities of ~7.8–20 m (frequencies of ~0.05–0.13 1/m; Fig. 4A-B; evolutionary spectral analysis: Fig. S1), which is in agreement with the visual observations. Bandpass filtering shows that the extracted ~7.8–20-m cyclicity follows significant maxima and minima in the GD and MS data (Fig. 5A-B). The filtered GD and MS components are consistent in terms of their phasing, especially between 0 and ~150 mbs, with filtered GD minima corresponding to filtered MS minima.

3.2. Time domain

The data was converted from the depth domain to the time domain using the Bayesian age model of Deino et al. (2021); Fig. 5C-D). Average sedimentation rates vary from ~13 to ~45 cm/kyr (i.e., a difference by a factor of ~3.5), meaning that the data was significantly distorted in the depth domain (Fig. S1). Sedimentation rates were lowest in the middle-upper part of the core (~101–77 mbs), while they were relatively high in the lower part of the core (~228–127 mbs) and highest in the upper, diatomite-dominated part of the core (~77–0 mbs).

Spectral analysis of the GD and MS data shows significant (>95 % CL) spectral power at <50 kyr periodicities (>0.02 1/kyr frequencies; Fig. 4C-D). The power spectrum of the MS data is dominated by a spectral peak focused around a period of ~40 kyr (frequency of ~0.025 1/kyr), which also occurs in the power spectrum of the GD data. Bandpass filtering of ~40 kyr periodicity in the MS and GD data shows that this cycle follows significant maxima and minima in the GD and MS data and that the phasing of this cycle is consistent between GD and MS (Fig. 5C-D). One minor difference is that the filtered MS component picks up an additional, low-amplitude cycle at ~2.77 Ma, which is not present in the filtered GD component. The filtered ~40 kyr components correspond well to the astronomical solution of obliquity (Fig. 5E), as the number of cycles in the GD data exactly matches the number of cycles in the obliquity solution. Both filtered ~40 kyr components display their greatest amplitudes in the interval around ~3.05 Ma,

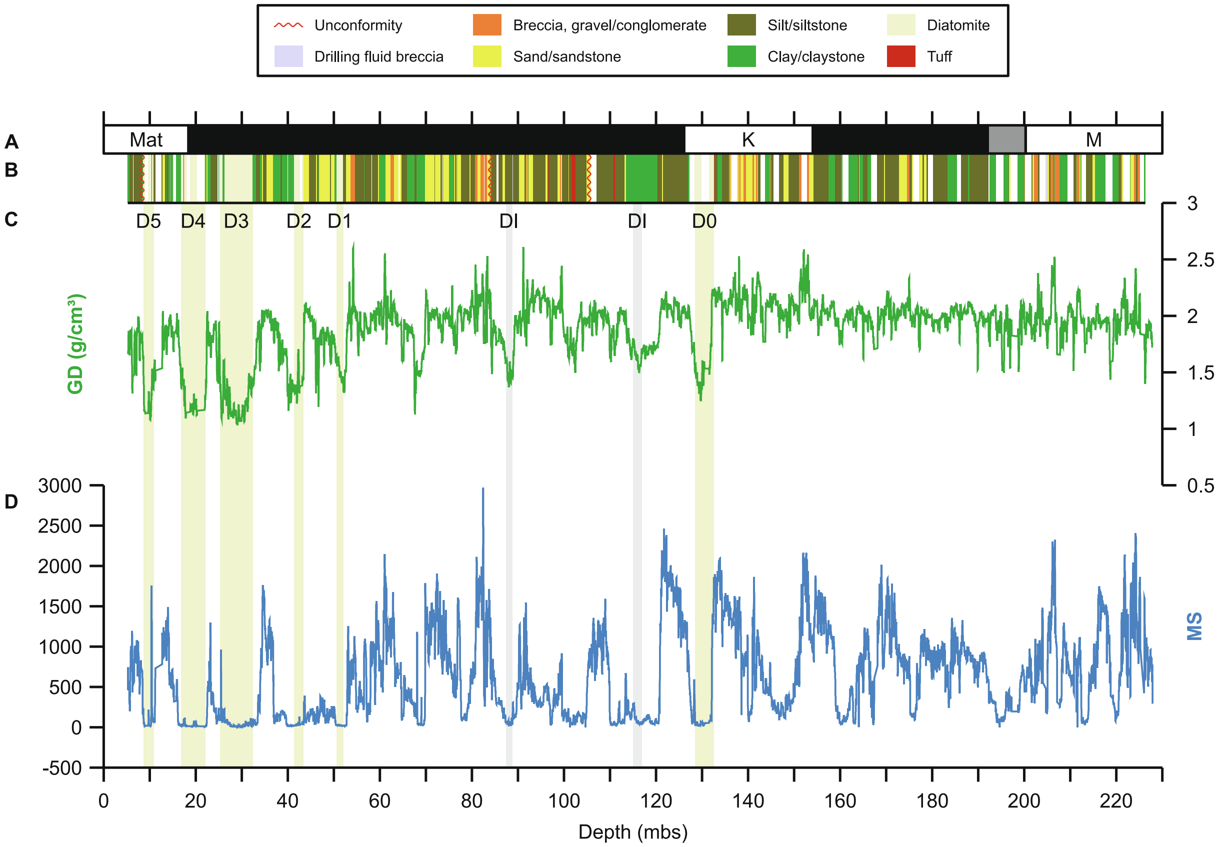

Fig. 3. Overview of BTB13 data in the depth domain: magnetostratigraphy (A; Sier et al., 2021) lithostratigraphy (B), GD (C), and MS (D; Cohen et al., 2016). Diatomites are indicated by the yellow-beige bars (Deino et al., 2021) and diatom-rich intervals are indicated by the grey bars (Westover et al., 2021). Abbreviations magnetostratigraphy: M = Mammoth, K = Kaena, Mat = Matuyama. (For interpretation of the references to colour in this figure legend, the reader is referred to the web version of this article.)

followed by a decrease in amplitude towards ~2.8 Ma. The amplitudes of the filtered cycle are again high around ~2.65 Ma for MS and ~2.73 Ma for GD. These variations in amplitude do not match with the amplitude variation of obliquity, which indicates a gradual increase in amplitude from ~3.05 to ~2.65 Ma. Instead, higher filtered ~40 kyr cycle amplitudes occur during or near 405 kyr eccentricity maxima (Fig. 5E).

Spectral analysis of the upper, diatomite-dominated part of the core (2.57–2.73 Ma) reveals that the GD and MS data in this interval are dominated by spectral power focused around a period of ~22 kyr (frequency of ~0.045 1/kyr; Fig. 4E-F). The GD and MS filtered ~22 kyr components have a similar phasing and their minima systematically concur with diatomites (Fig. 5F-G). The filtered ~22 kyr cycles compare well with the precession solution (Fig. 5H), as they contain a similar amount of cycles in this interval. This ~22 kyr-paced interval occurs during a 405 kyr eccentricity maximum, within a ~2.4 Myr eccentricity minimum (Fig. 5E).

4. Astronomical tuning

The results from spectral analysis indicate that the GD and MS data display significant variability at scales of ~40 kyr and ~22 kyr. These periodicities are very close to those of obliquity (41 kyr) and precession (19, 22, and 24 kyr), and therefore very likely linked to these astronomical cycles.

4.1. Initial obliquity tuning

As the obliquity signal is dominant throughout the record, we first astronomically tune the data to obliquity. Analysis of the coherence and phase indicates that filtered ~40 kyr cycle minima correspond best with obliquity maxima (i.e., the two are out of phase; Fig. 6A-D). Therefore, for a first tuning we assume that this phasing is correct and that there is a minimal offset with the Bayesian age model. When correlating the first and last filtered ~40 kyr cycle minima to their closest obliquity maxima, the number of filtered ~40 kyr cycles in between matches with the number of obliquity cycles. Compared to GD, the filtered ~40 kyr cycle of MS picks up an extra, but very low-amplitude cycle around ~2.77 Ma, which suggests that the data is still somewhat distorted in this interval. Tie-points were determined by averaging the ages of GD and MS filtered ~40 kyr cycle minima (Fig. 6E). Subsequently, the ages of the tie-points were converted to depth by inverting the Bayesian age model of Deino et al. (2021). The tie-points were tuned to their corresponding obliquity maxima (Fig. 6F; Table A.1).

Spectral analysis on the obliquity-tuned GD and MS data reveals that the most significant (>95 % CL) spectral peak is centered around a period of ~41 kyr (Fig. 7A-B), which is expected as the data is tuned to obliquity. Bandpass filtering of the ~41 kyr cyclicity indicates a consistent phasing between GD, MS, and obliquity, with only very minor phase differences due to differences in the variability of GD and MS (Fig. 7C-E). Additionally, significant (>95 % CL) spectral power occurs around a period of ~24 kyr for GD and ~22 kyr for MS, coinciding with the periods of precession (19, 22, and 24 kyr; Fig. 7A-B). For MS the spectral peak is well-defined and falls exactly between the precession periods, while for GD spectral power occurs in a somewhat broader range extending to periods >24 kyr.

4.2. Precession tuning

The significant spectral power that is present around the precession

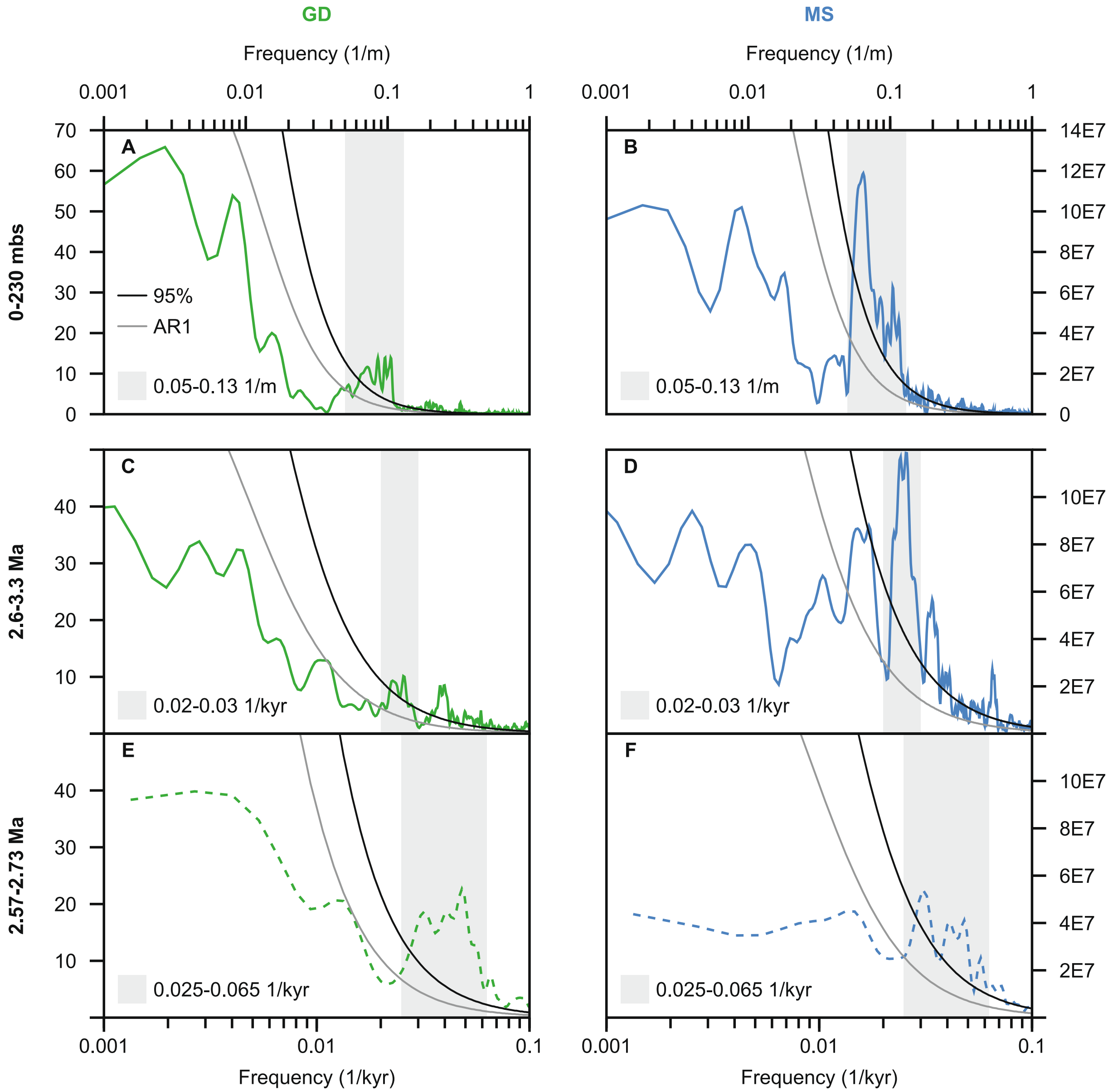

Fig. 4. Spectral analysis of GD and MS data in depth domain (A-B) and time domain using the Bayesian age model for the entire interval (C—D) as well as the upper diatomite-rich interval separately (*E*-F).

frequencies in the obliquity-tuned data provides an opportunity to further improve the astronomically-tuned age model. Therefore, we also astronomically tune the data to precession. To accurately capture the precession signal and reduce the influence of distortions that are likely still present at this scale, a relatively broad filter width (0.03–0.07 1/kyr) is chosen. Analysis of the coherence and phase on the obliquity-tuned MS data indicates that filtered ~20 kyr cycle minima correspond best with precession minima (i.e., the two are in phase; Fig. 8A-B). Tie-points were placed at the filtered ~20 kyr cycle minima (Fig. 8C), converted to depth using the inverted obliquity-tuned age model, and correlated to their corresponding precession minima while also comparing patterns in the data to the sum of standardized eccentricity, obliquity and precession weighted with 0, 1 and -1, respectively (0E1T-1P curve; Fig. 8D-E; Table A.2).

The filtered ~20 kyr cycle generally shows a good correspondence to the 0E1T-1P and precession curves. However, it picks up two cycles instead of one around ~2.68 Ma and ~2.77 Ma, picks up an extra cycle in the broad MS minima around ~2.93 Ma and ~3.19 Ma, and picks up only one cycle instead of two around ~3.22 Ma. It also does not pick up a clear cycle around ~2.82 Ma, but as the amplitude of precession is very small here, this is actually in good correspondence with the 0E1T-1P curve. The tie-points related to the discrepancies were not used for the precession tuning (grey dotted lines in Fig. 8).

Spectral analysis on the precession-tuned GD and MS data reveals significant (>95 % CL) spectral power around ~41 kyr and ~22–24 kyr (Fig. 9A-B). Compared to the obliquity-tuned data, spectral power around ~22–24 kyr is much higher for MS and only somewhat higher, but more centered, for GD. Although the data is now only tuned to precession, spectral power around ~41 kyr is similar for both the obliquity- and precession-tuned data. Bandpass filtering of the ~41 kyr cyclicity indicates that the fit between both datasets and the obliquity solution is very good, even better than the fit for the obliquity-tuned data (Fig. 9E). The filtered ~22–24 kyr cyclicity in the MS data follows the 0E1T-1P and precession curves very well (Fig. 9F-G). Only minor discrepancies occur around ~3.22 Ma, which corresponds to an intervals where tie-points where left out (Fig. 8C-E).

The amplitude variations of the filtered ~22–24 kyr cycle are very similar to those in the 0E1T-1P curve (Fig. 9F), indicating that the signal

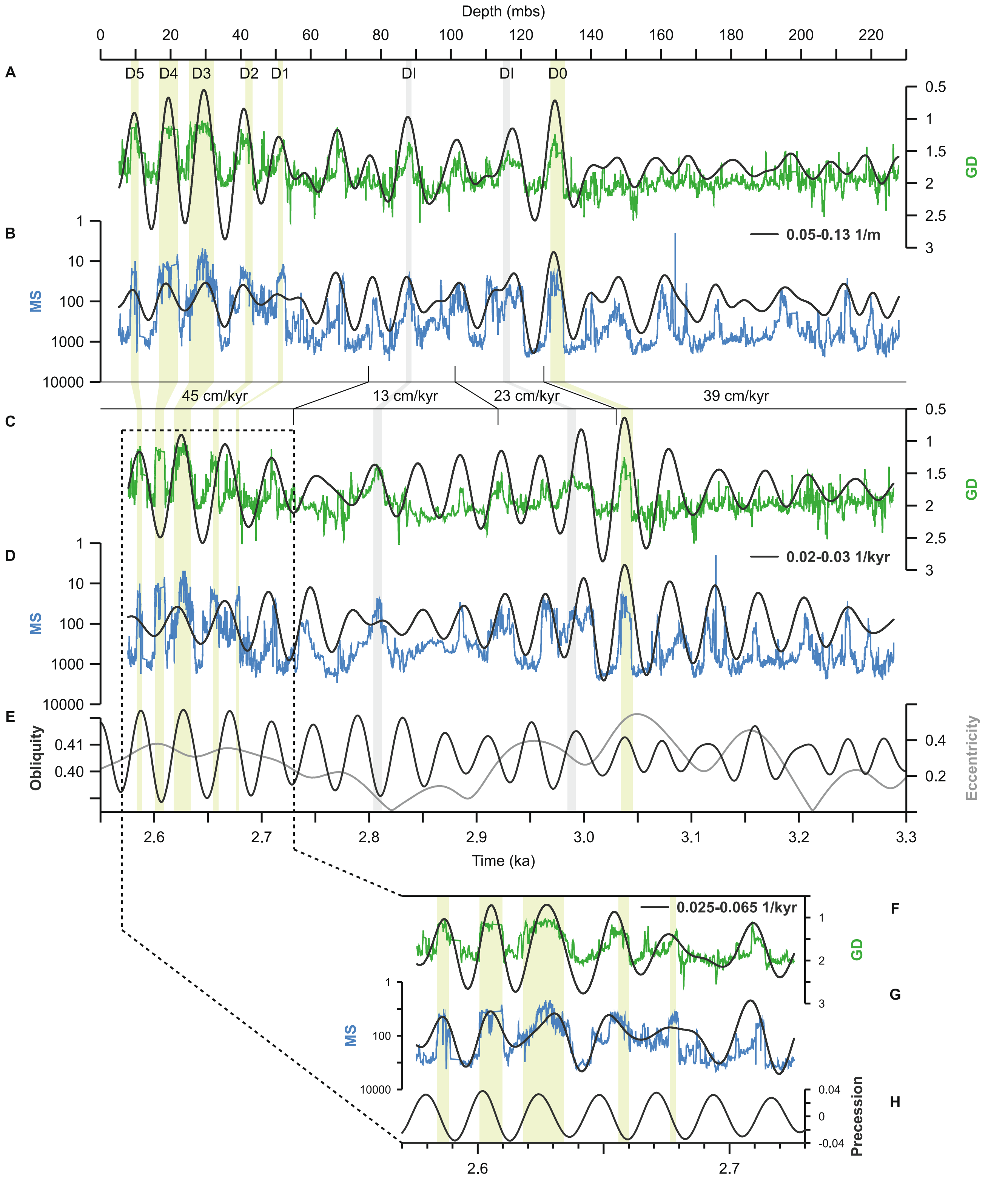

Fig. 5. Overview of bandpass filtering of GD and MS in depth domain (A-B) and time domain using the Bayesian age model for the entire interval (C—D) as well as the upper diatomite-rich interval separately (F-G). The filtered cycles are compared to eccentricity and obliquity (E), and precession (H). GD and MS data are plotted on a reversed y axis, and MS is plotted on a logarithmic scale. Diatomites are indicated by the yellow-beige bars and diatom-rich intervals are indicated by the grey bars.

represents an interference pattern between precession and obliquity. Indeed, the amplitude modulation (AM) of the filtered ~22–24 kyr cycle is consistent with the AM of the 0E1T-1P curve (Fig. 10A), representing precession-obliquity combination tones with a main periodicity of ~50–60 kyr (Spiering et al., 2024). Larger-scale variations in amplitude, represented by the envelope of the AM of the filtered ~22–24 kyr cycle, follow the 405 kyr eccentricity cycle relatively well (Fig. 10B). Surprisingly, the AM of the filtered ~41 kyr MS cycle also follows the ~405

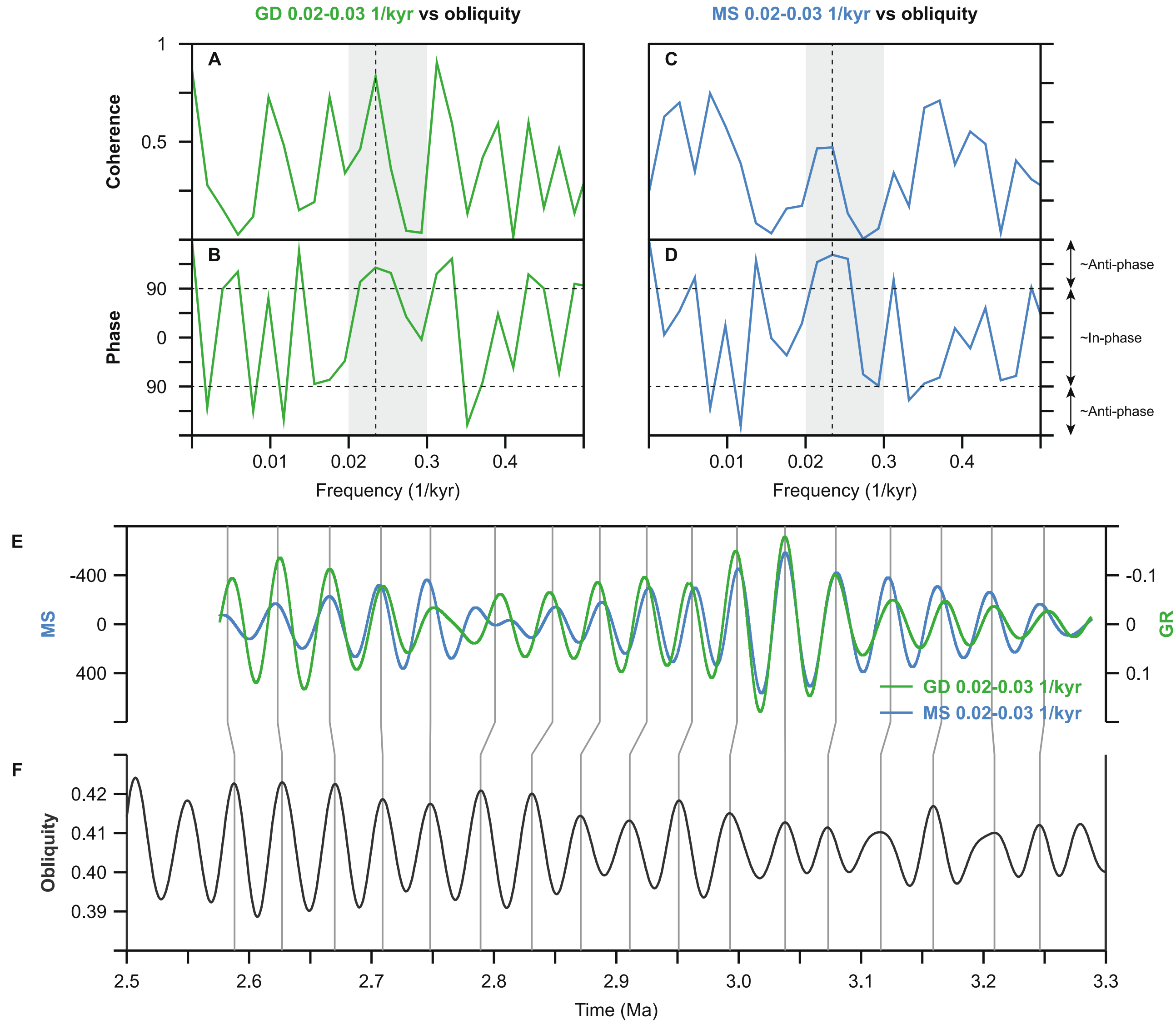

Fig. 6. Coherence and phase between Bayesian age model filtered MS and GD and obliquity (A-D). Grey bars indicate bandpass filter widths. Astronomical tuning of GD and MS to obliquity (E-F). Tie-points are indicated by the grey lines.

kyr eccentricity cycle relatively well, especially between ~2.8 and ~3.3 Ma (Fig. 10B). This suggests that the amplitude of the filtered obliquity signal was related to AM of precession (i.e., eccentricity) instead of AM of obliquity, possibly as a result of the precession-obliquity interference recorded in the data.

4.3. Final 0E1T-1P tuning

The precession tuning presented above independently showed the strong presence of obliquity in the data. The inferred precession-obliquity interference patterns picked up by the filtered ~20 kyr cycle match very well with the interference patterns in the 0E1T-P curve. A shift of half a precession cycle, one precession cycle (~half an obliquity cycle), or two precession cycles (~one obliquity cycle) would result in a worse fit of these interference patterns. This indicates that the assumed phase relationships are correct, that the offset with the Bayesian age model is indeed minimal, and that no iteration steps are required. As our analysis revealed the presence of precession-obliquity interference, and as precession minima slightly differ in age from 0E1T-1P maxima, we present a final age model based on the tuning of filtered ~20 kyr MS cycle minima to 0E1T-1P maxima. We use the filtered ~20 kyr cycle of the precession-tuned age model instead of the obliquity-tuned age model to reduce the influence of any remaining distortions. Tie-points were placed at the precession-related filter minima (Fig. 11A), converted to depth using the inverted precession-tuned age model, and correlated to their corresponding 0E1T-1P maxima (Fig. 11B; Table A.3). The minimum in the filtered data at ~2.81 Ma is not used as tie-point as there is no maximum in the 0E1T-1P curve due to the very low precession amplitude. The 0E1T-1P maximum at ~3.23 Ma is not used as tie-point as there is no clear minimum in the filtered data. Spectral analysis and bandpass filtering is similar as for the precession-tuned age model (Fig. 12). Besides power around the regular astronomical frequencies, the spectrum displays significant power around ~9–12 kyr, ~7 kyr, and ~4–5 kyr (Fig. 13A). Bandpass filtering indicates that the ~9–12 kyr cycle follows MS variations in most of the record and therefore does not represent a harmonic (Fig. 13B).

5. Discussion

The cyclostratigraphic analyses and development of an astronomically-tuned age model indicates that the BTB13 site was significantly influenced by precession and obliquity during the interval from ~3.3 to ~2.6 Ma. This is in agreement with previous interpretations of the variability in the BTB13 core and in outcrop sections

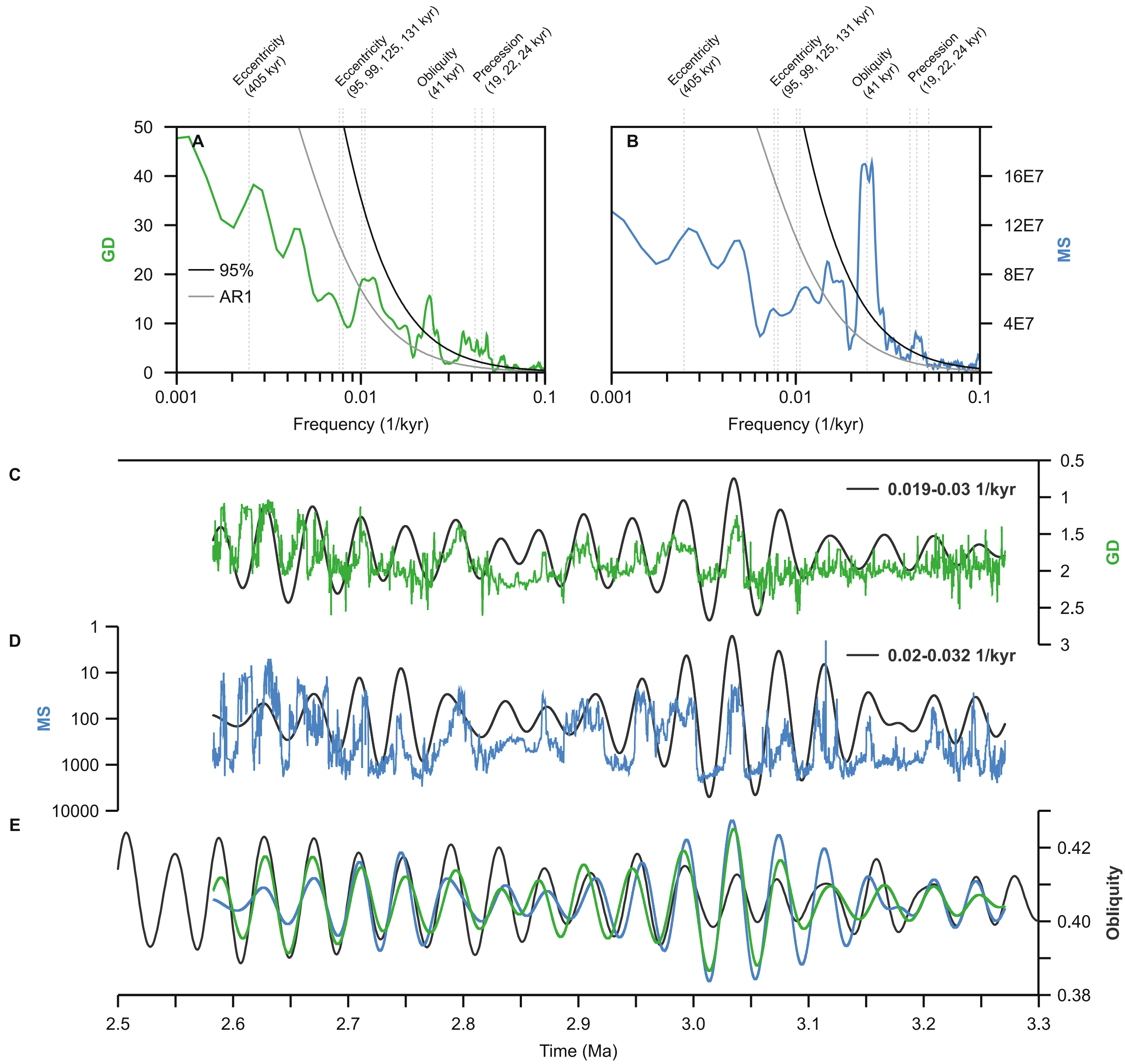

Fig. 7. Spectral analysis (A-B) and bandpass filtering (C—D) of obliquity-tuned GD and MS data, and comparison to obliquity (E).

of the Chemeron Formation (Deino et al., 2006; Kingston et al., 2007; Mitsunaga et al., 2023). The final 0E1T-1P-tuned age model provides a very good fit with the astronomical solution and is consistent with most of the independent age control points at the 1-sigma uncertainty range (Deino et al., 2021; Fig. 2B). It is not consistent with the alternative 'unconformity scenario' in which ~40 kyr is missing at ~105 mbs (Deino et al., 2021), as a shift in the tuning of one obliquity, or even precession cycle, would result in a misfit with the precession-obliquity interference patterns (i.e., the 0E1T-1P curve). Our cyclostratigraphic analysis suggests that all precession cycles are recorded and no hiatuses with a duration of more than a precession cycle (i.e., >22–24 kyr) are present.

5.1. Phase relationship

For the astronomical tuning, we assumed that GD and MS minima are related to obliquity maxima and precession minima. Although this was supported by the statistical analysis of the coherence and phase between the filtered data and the astronomical solution, these outcomes could be significantly affected by uncertainties in the Bayesian age model. A more persuasive argument is provided by the very good fit with precession-obliquity interference. As this interference forms a unique pattern, such a good fit cannot be maintained when shifting the age model by half or one obliquity or precession cycle.

The assumed phasing is consistent with previous interpretations based on the group of five diatomites in outcrop (Deino et al., 2006; Kingston et al., 2007), which in-core concur with GD and MS minima. The ages of these diatomites were calculated using linear interpolation between astronomically-calibrated $^{40}Ar/^{39}Ar$ ages, which resulted in an almost perfect fit between diatomites and boreal summer insolation maxima (i.e., precession minima; Deino et al., 2006; Fig. 14A). For the core, however, the fit between the calculated diatomite ages and precession minima is less persuasive, with some diatomites occurring in between insolation maxima and minima or closer to minima (Fig. 14B-C). The difference resulted from a combination of lateral variations in diatomite thickness, recalculation of $^{40}Ar/^{39}Ar$ ages with a different decay constant and slightly younger, astronomically-calibrated Fish Canyon sanidine age (Kuiper et al., 2008), and the use of a Bayesian

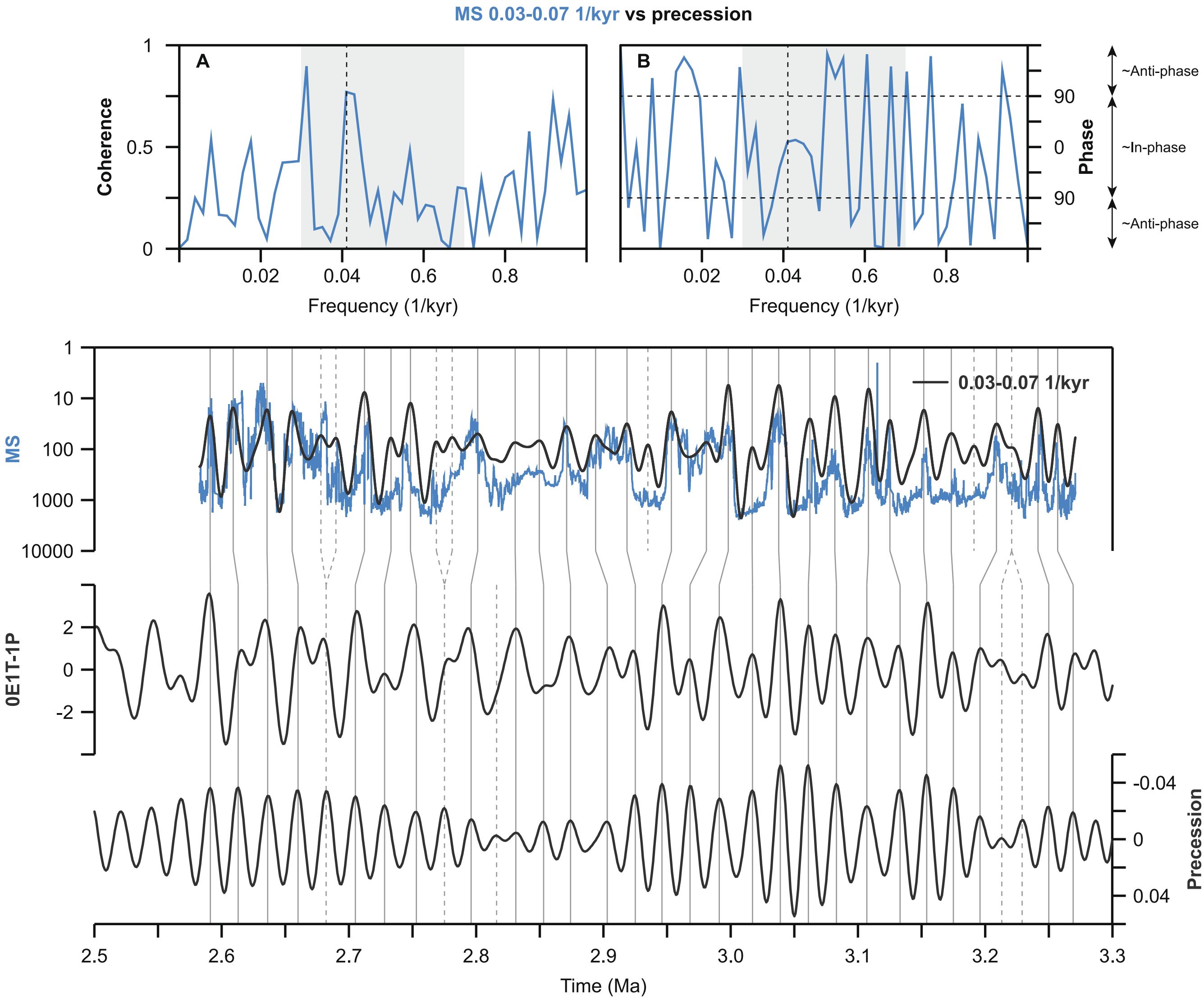

Fig. 8. Coherence and phase between obliquity-tuned filtered MS and precession (A-B). Grey bars indicate bandpass filter width. Astronomical tuning of MS to precession (C-E). Tie-points are indicated by the grey lines. Dotted grey lines are not used as tie-points.

approach instead of linear interpolation between $^{40}Ar/^{39}Ar$ ages (Deino et al., 2021). Besides the external factors, internal errors of the $^{40}Ar/^{39}Ar$ ages are generally too large to confidently determine the precession phasing (the median 1-sigma error is ~7–9 kyr, which is more than a quarter precession cycle; Deino et al., 2021).

Alternatively, if the magnetostratigraphy is of excellent quality, one could use astronomically-tuned ages of the paleomagnetic reversal boundaries identified within D4 and just above D0 to correlate the diatomites to precession. Unlike diatomites D1–5, the older D0 does exactly correspond to a boreal summer insolation maximum based on the Bayesian age model (Deino et al., 2021). However, there could be uncertainties in the exact placement of the reversal boundaries due to the difficulties of magnetostratigraphy on low-latitude drill cores (Sier et al., 2021; Deino et al., 2021), and for the Gauss-Matuyama boundary there is still some ambiguity in the exact astronomical age (Channell et al., 2020).

By coincidence or not, the $^{40}Ar/^{39}Ar$-inferred diatomite insolation phasing does make sense from a palaeoclimatological perspective. As diatom assemblages indicated that the diatomites represent deep and extensive lake phases, they were interpreted as wet phases related to strengthening of the North African monsoon in response to increased boreal summer insolation (Deino et al., 2006; Kingston et al., 2007). Modeling studies indicated that boreal summer insolation maxima result in a significant increase in precipitation over the African continent focused around ~10–15°N, but also extending towards ~0°, both in western and eastern Africa (Bosmans et al., 2015a). The Baringo paleolake could have been affected by river runoff coming from low northern latitudes in eastern Africa. For example, the main water source of the nearby Lake Turkana is the Omo River (Johnson and Malala, 2009), which originates in the Ethiopian Highlands.

Alternatively, deep lake phases could be related to maxima in direct equatorial insolation instead of maxima in boreal summer insolation. The modern-day East African Rift valley experiences two rain seasons, the ‘long rains’ in March and the ‘short rains’ in September (Deino et al., 2006), which occur when equatorial insolation reaches its maximum during the spring and autumn equinoxes. In the present-day, equatorial insolation is slightly higher in March compared to September, but this relationship changes through time due to precession as perihelion is reached in different months (Berger et al., 2006). In this case, the system is expected to generate half (and quarter) precession cycles as well as strong ~100 and 405 kyr eccentricity cycles (Berger et al., 2006). Half-precession cycles of ~10–12 kyr have been observed in proxy records from other lakes in equatorial Africa (e.g., Lake Challa: Verschuren et al., 2009; Lake Bosumtwi: Vinnepand et al., 2024; Kenya Rift Lakes:

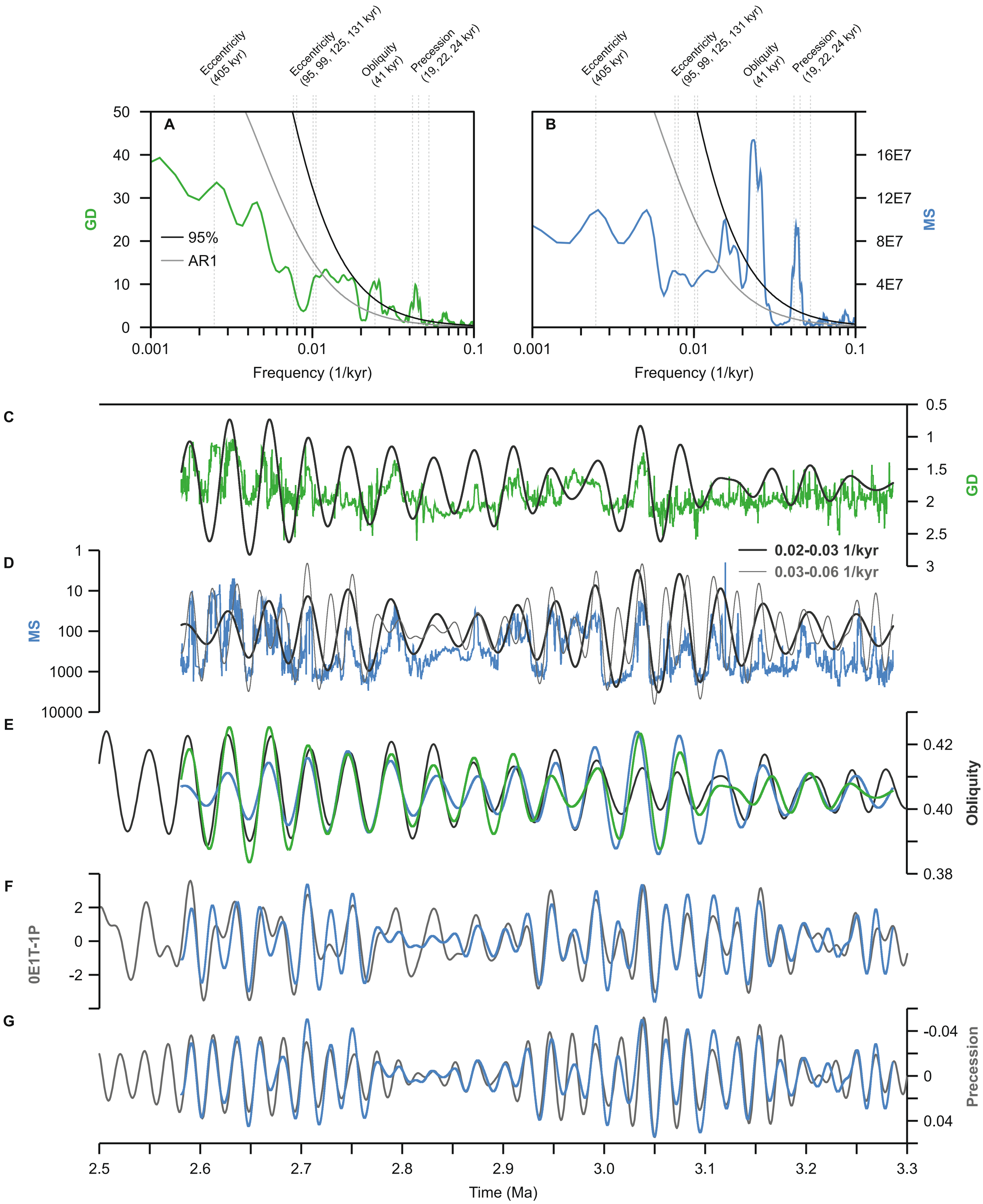

Fig. 9. Spectral analysis (A-B) and bandpass filtering (C—D) of precession-tuned GD and MS data, and comparison to obliquity (E), 0E1T-1P (F), and precession (G).

Trauth et al., 2003). The tuned BTB13 data also displays significant spectral power around periodicities of ~9–12 kyr, possibly representing half precession, as well as some more isolated spectral peaks around ~4–6 kyr, possibly representing quarter precession (Fig. 13). However, no significant peaks are found in the eccentricity band of the spectrum (Fig. 12A-B). As the precession signal is much stronger than the potential half and quarter precession signals, the most logical interpretation is that the recorded wet phases were related to boreal summer insolation maxima, and therefore precession minima and obliquity maxima. Direct equatorial insolation might have had a secondary influence.

5.2. *Comparison to Mediterranean sapropels*

As the BTB13 site was likely influenced by the North African monsoon, we compare the data to the summer inter-tropical insolation gradient, which is the most representative reference curve for the North African monsoon (Bosmans et al., 2015b), and the Mediterranean sapropel record from the Punta Piccola section (Hilgen, 1991; Fig. 1;

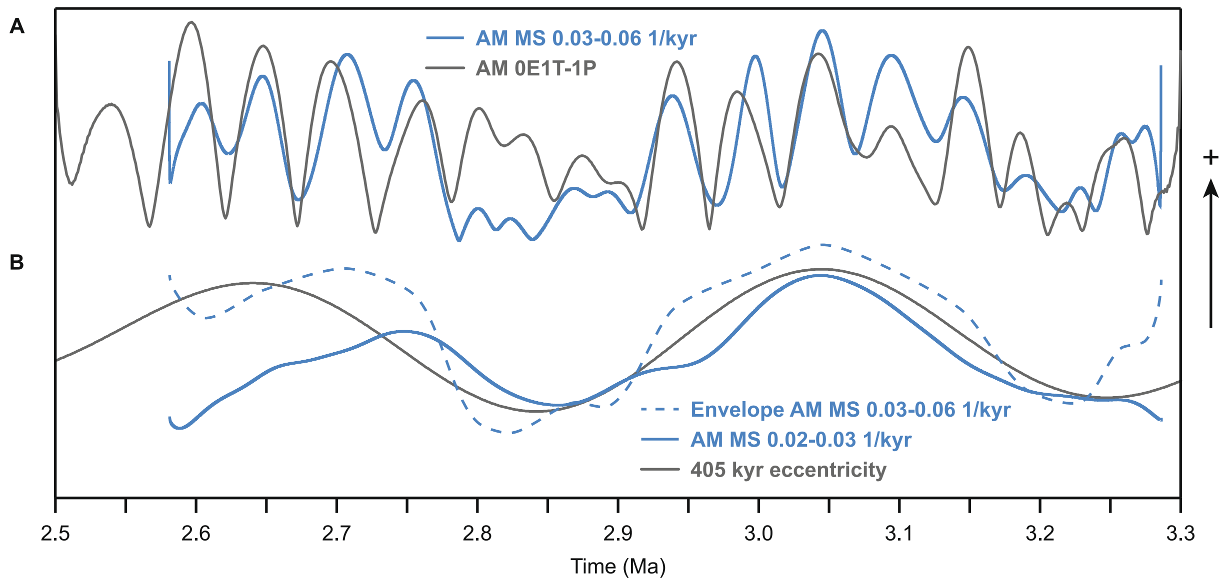

Fig. 10. Amplitude modulation of precession-tuned MS bandpass filtering and comparison to the astronomical solution (A-B).

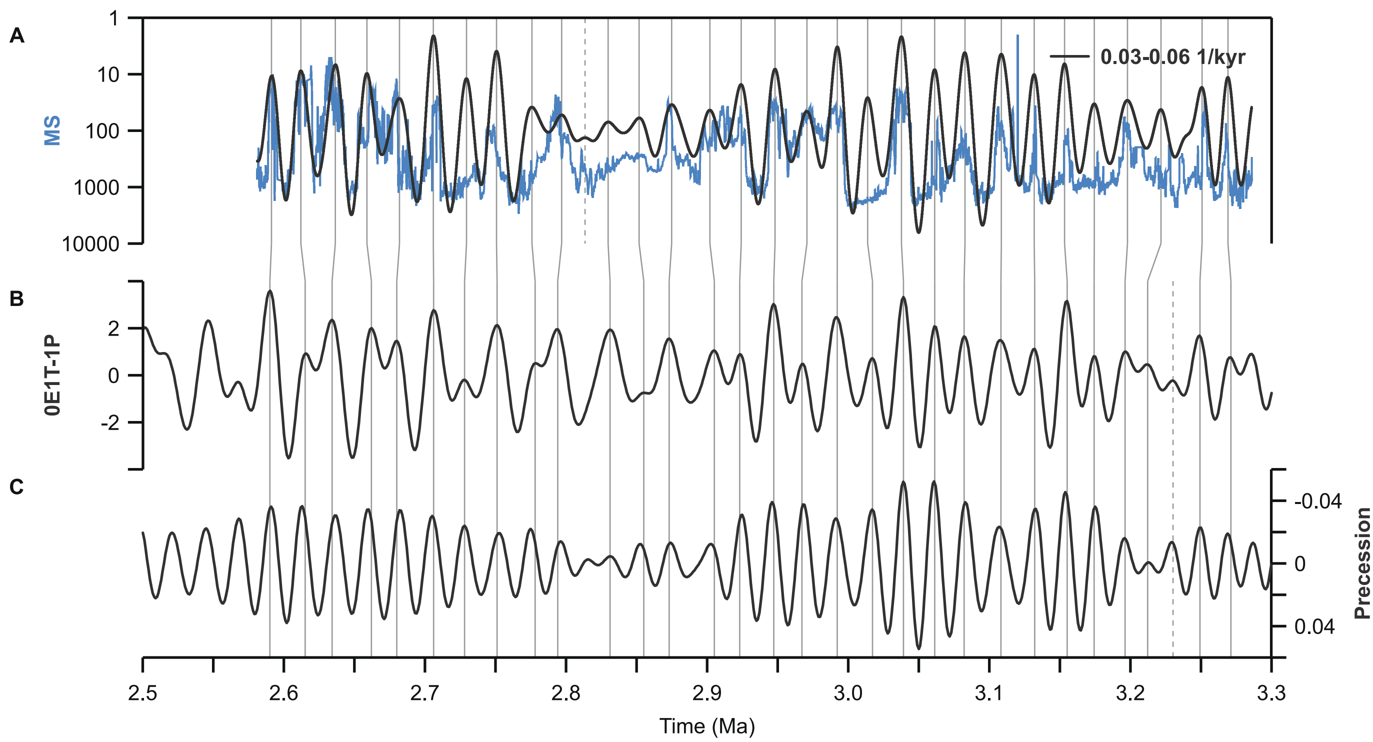

Fig. 11. Final astronomical tuning of MS to the 0E1T-1P curve (A-C). Tie-points are indicated by the grey lines. Dotted grey lines are not used as tie-points.

Fig. 15). The GD and MS minima that concur with diatomites likely represent the most extreme wet phases in the core and therefore the most extreme insolation forcing. This occurs during precession minima and obliquity maxima, when Earth resides in perihelion during boreal summer and when the tilt of the Earth's axis is increased. This configuration is expected to have resulted in sapropel formation in the Mediterranean due to increased Nile river runoff as a consequence of more extreme northward displacement of the Intertropical Convergence Zone (ITCZ) and intensification of the North African monsoon.

The single-occurring older diatomite D0 is correlated to the strongest insolation gradient maximum at 3038 ka, which corresponds to a precession minimum within an obliquity maximum, a ~100 kyr eccentricity maximum, and a 405 kyr eccentricity maximum. In the Mediterranean Punta Piccola record, D0 correlates to the second-oldest sapropel (cycle 103) within the oldest group of sapropels (cycles 102–103; Hilgen, 1991). No diatomites are associated with the other sapropels around this 405 kyr eccentricity maximum. This suggests that, even though these sapropels indicate that conditions were relatively wet, the insolation forcing was apparently not high enough for diatomites to form during these times. The interval between D0 and D1 corresponds to a period of lower eccentricity related to a 405 kyr eccentricity minimum. This configuration results in less extreme variations in precession and therefore a more obvious influence of obliquity on insolation gradient changes, which is reflected in both the BTB13

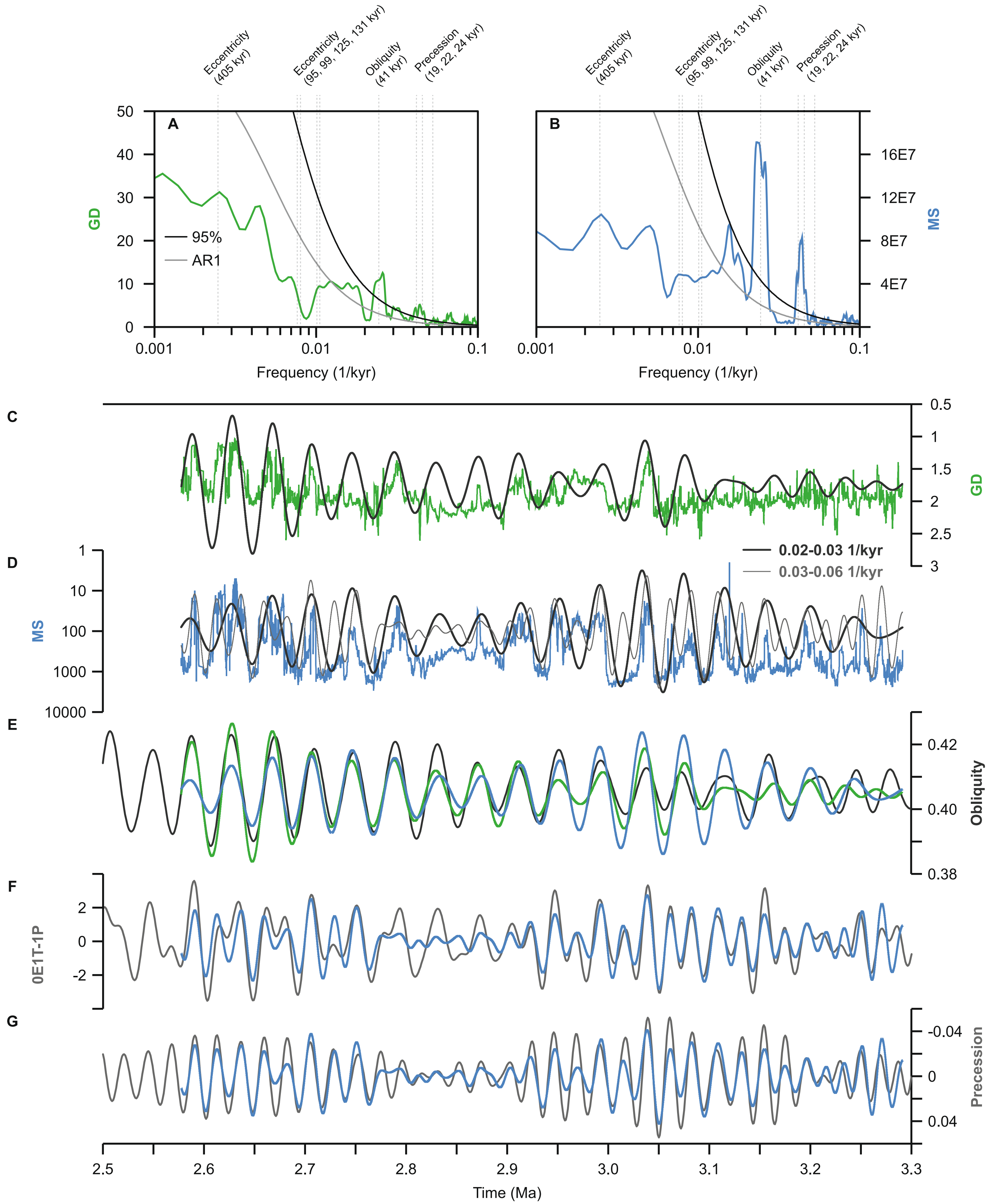

Fig. 12. Spectral analysis (A-B) and bandpass filtering (C—D) of 0E1T-1P-tuned GD and MS data, and comparison to obliquity (E), 0E1T-1P (F), and precession (G).

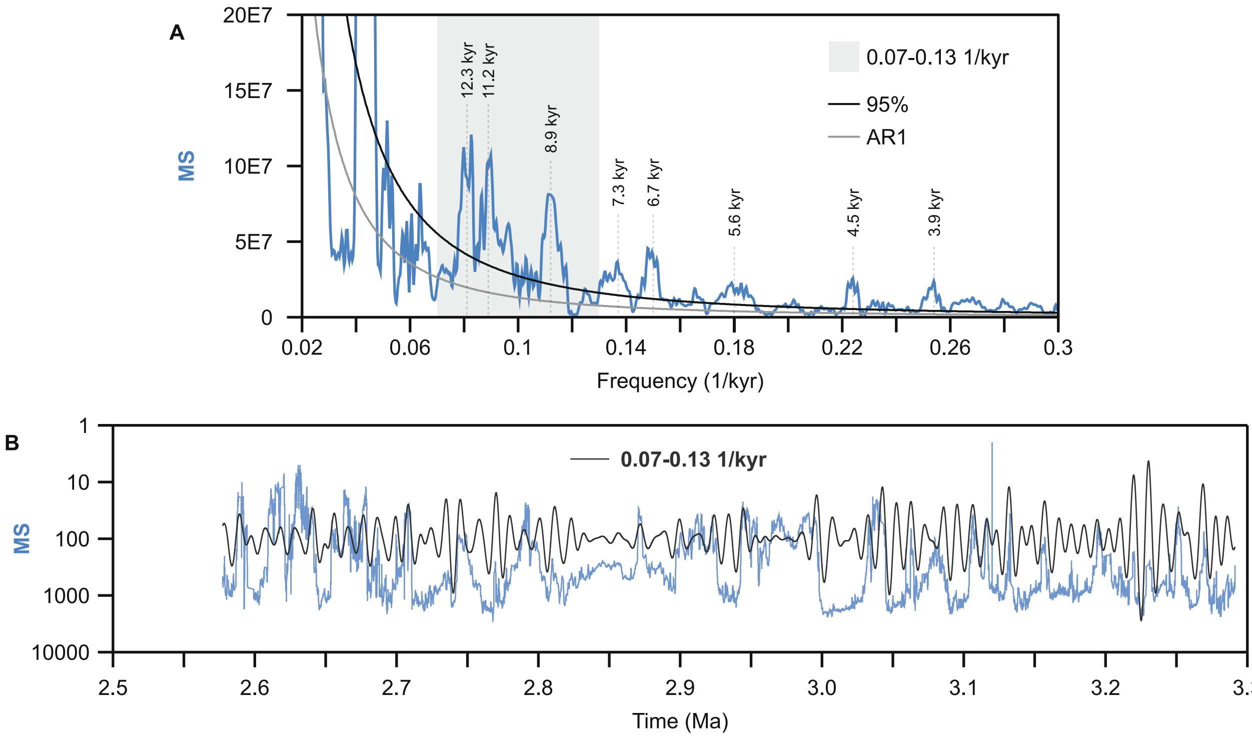

Fig. 13. Spectral analysis and bandpass filtering of 0E1T-1P-tuned MS data focused on sub-Milankovitch frequencies.

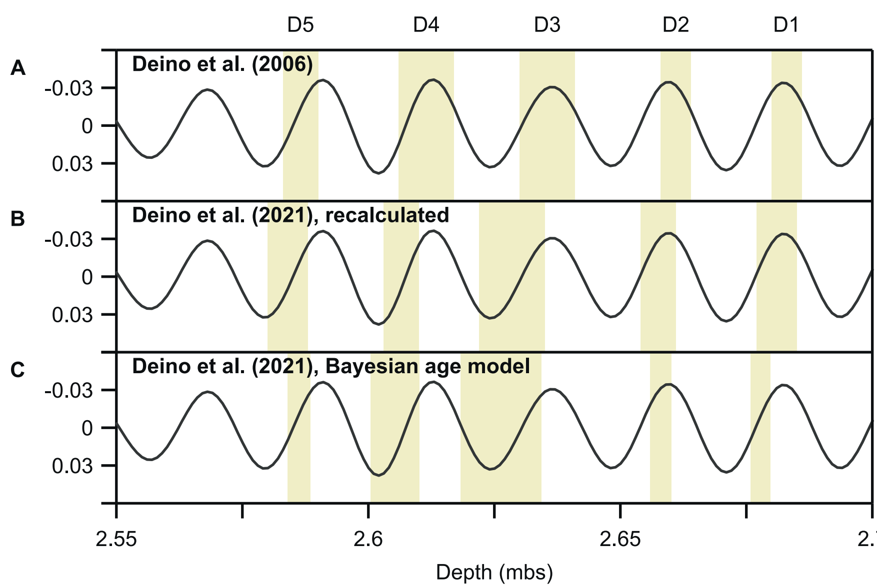

Fig. 14. Diatomite ages (yellow-beige bars) versus precession (black line) based on initial astronomically-calibrated $^{40}Ar/^{39}Ar$ ages (Deino et al., 2006; A), recalculated $^{40}Ar/^{39}Ar$ ages (Deino et al., 2021; B), and the Bayesian age model (Deino et al., 2021; C).

datasets and the Punta Piccola section.

In the top of the core, the group of five diatomites (D1–5) are correlated to the insolation gradient maxima at 2681, 2660, 2635, 2613, and 2590 ka, which are all relatively strong as they occur within a 405 kyr eccentricity maximum. In the Punta Piccola section, the diatomites correlate to the upper five sapropels of a group of six (cycles 115–119; Hilgen, 1991). There is no corresponding diatomite for the first sapropel of this group. This sapropel group forms an aberrant pattern that is related to the node (minimum) in the 2.4 Myr eccentricity cycle around 2.6–2.7 Ma when the expression of short eccentricity is strongly reduced. Here, diatomites also formed during insolation gradient maxima that are lower than the one correlated to D0, suggesting that the threshold for diatomite formation was lowered during this period. This could be related to the shift towards wetter conditions inferred from leaf wax *n*-alkane hydrogen isotope data from the BTB13 core (Mitsunaga et al., 2023). However, as this shift is observed around 3 Ma, diatomites would be expected at the relatively high insolation gradient maxima around ~3–2.95 Ma, which is not the case. Also, diatomites do not always correspond to the lowest hydrogen isotope values (Fig. 5 of Mitsunaga et al., 2023), suggesting that the two might be representing somewhat different aspects of the regional hydrological system.

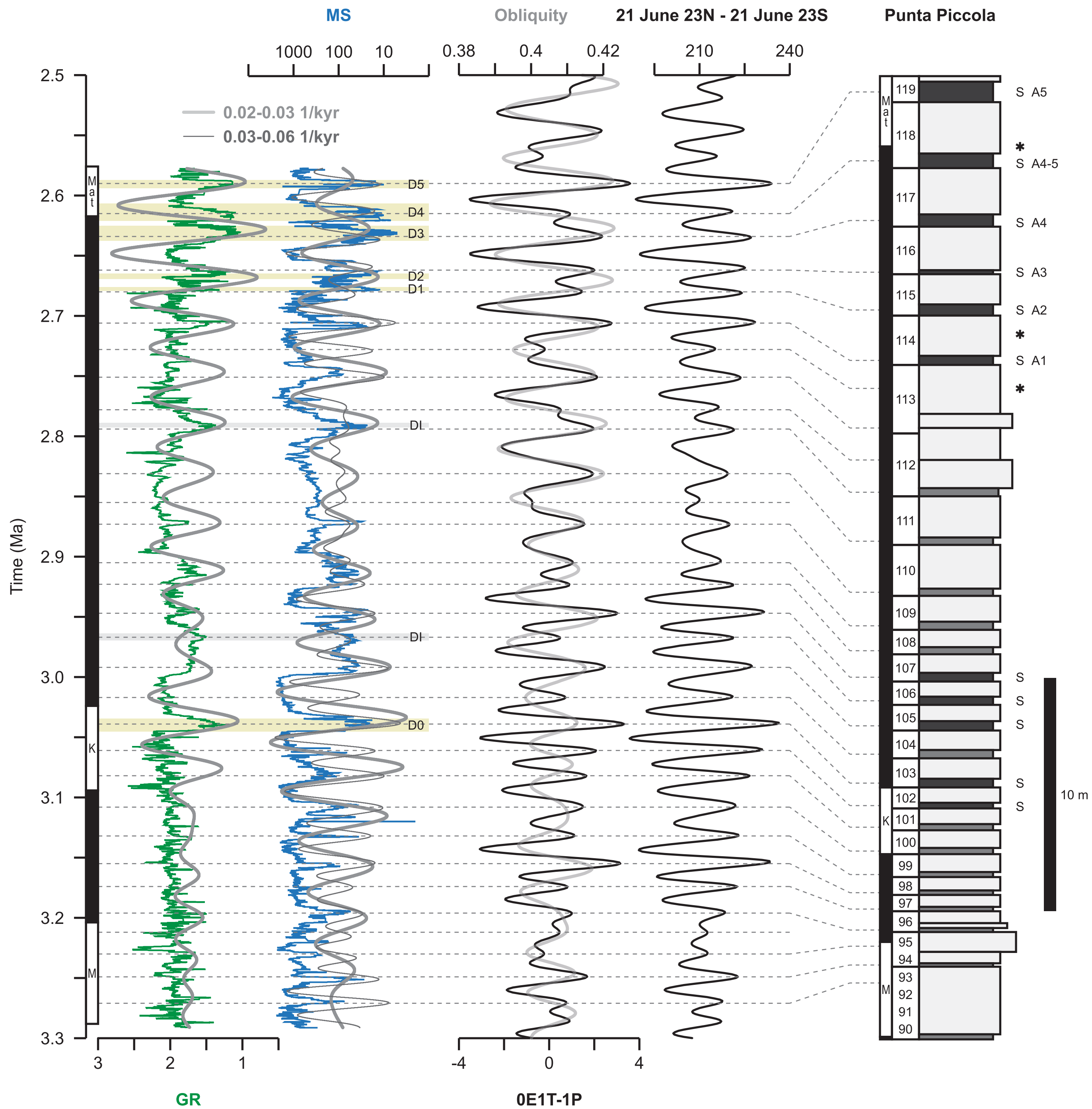

Fig. 15. Comparison of 0E1T-1P-tuned BTB13 data to the astronomically-tuned Mediterranean sapropel record of the Punta Piccola section (Hilgen, 1991). Diatomites are indicated by the yellow-beige bars, diatom-intervals by the grey bars, and tuning tie-points by the dotted grey lines. Abbreviations magnetostratigraphy: M = Mammoth, K = Kaena, Mat = Matuyama. Abbreviations Punta Piccola section: S = sapropel.

5.3. Origin of obliquity dominance

There is a remarkable dominance of obliquity and relatively weak expression of precession, particularly in the pre-2.7 Ma part of the record, which is not easily explained for low latitudes. This obliquity dominance was also observed in leaf wax *n*-alkane hydrogen isotope data from the BTB13 core (Mitsunaga et al., 2023). Curiously, the precession-related diatomite cycles in the top 55 mbs of the core have the same thickness as the older cycles of inferred obliquity origin. This is caused by distortion in the stratigraphic domain related to the high sedimentation rate in the top part of the core compared to lower sedimentation rates in the lower and, particularly, middle part of the core (Fig. 5; Deino et al., 2021). However, as the initial age model is of high-quality and is built independent from the astronomical tuning, this shift in sedimentation rate is likely not an artefact. Another potential explanation is that these pre-2.7 Ma cycles are also related to precession, but that half of the cycles were not deposited or were removed by erosion in multiple or cyclic hiatuses. However, this explanation is not very likely in view of the consistent patterns found in the cyclicity.

The insolation forcing of the North African monsoon is not only controlled by precession but also by obliquity as the insolation forcing of the monsoon does not only depend on low-latitude boreal summer insolation, but on a low-latitude insolation gradient that includes southern latitudes (Bosmans et al., 2015b). A stronger interhemispheric insolation contrast drives a stronger winter Hadley circulation and, consequently, stronger cross-equatorial moisture transport from the winter hemisphere, where the influence of obliquity is larger, into the summer hemisphere (Mantsis et al., 2014). This mechanism has been independently confirmed by the outcome of climate modeling of precession and obliquity extremes (Bosmans et al., 2015a; Bosmans et al., 2015b) and was proposed as a possible origin for the strong obliquity signal in BTB13 leaf wax data (Mitsunaga et al., 2023). It may explain the presence of obliquity at low latitudes, but not the apparent dominance of obliquity as seen in the BTB13 core. We are looking at precession-obliquity interference patterns with a much stronger contribution of obliquity than for instance observed in Mediterranean sapropel records. There, the relative contribution of precession is larger than obliquity, which is in agreement with the insolation gradient held responsible for the variations in the intensity of the North African monsoon (Bosmans et al., 2015b). Yet, an obliquity dominance might be explained by a combined influence of this insolation gradient and the direct influence of equatorial insolation as mentioned before (section 5.1). The latter could decrease the strength of the precession signal (Berger et al., 2006), thereby making the obliquity signal relatively stronger. Moreover, an obliquity signal is also produced by the seasonal cycle of equatorial insolation (i.e., the curve of largest amplitude of insolation difference between equinoxes and solstices; Berger et al., 2006).

Lastly, a link to higher latitudes might explain the obliquity dominance at the equator. Mitsunaga et al. (2023) invoked a link to high-latitude austral cooling and changes in Indian Ocean temperature gradients to explain the inferred shift in eastern African hydroclimate at 3 Ma. One can argue that in this way also high-latitude glacial cyclicity, potentially dominated by obliquity, may exert an influence on low-latitude climate. A mid- to high-latitude forcing was also proposed to explain the dominance of obliquity in low-latitude proxy records from the eastern equatorial Atlantic (Spiering et al., 2024). As often is the case, this dominance occurred during a 2.4 Myr eccentricity minimum. However, for the BTB13 core obliquity dominance occurs before a 2.4 Myr eccentricity minimum, while the 2.4 Myr eccentricity minimum is associated with an increased influence of precession. The shift from obliquity to precession dominance coincides exactly with the intensification of Northern Hemisphere glaciations, although the climate response to this transition was shown to be complex and not globally synchronous (McClymont et al., 2023). It might seem counterintuitive that intensified, obliquity-driven glaciations result in a stronger precession and weaker obliquity signal in the BTB13 record. However, this could be explained by compression of the Intertropical Convergence Zone in response to ice expansion, which would make East Africa, and therefore the BTB13 site, more sensitive to precession forcing (Trauth et al., 2007).

5.4. Importance of regional astrochronological frameworks

We show that astronomical age models, with their unprecedented accuracy, precision and resolution, can also be established for continental successions that play an important role in reconstructing the evolutionary history of our species. However, this is not the first time that such an age model is presented. For example, Joordens et al. (2011) correlated a proxy record from Lake Turkana to astronomically-tuned sapropels in the Mediterranean for the interval between 2 and 1.85 Ma, while Hilgen et al. (2022) established two possible astronomical age models for the hominin-bearing succession in the Sangiran area in Indonesia. For the Sangiran section, the uncertainty in the tuning mainly resulted from uncertainties in the initial magneto-radio-isotopic age model (Hilgen et al., 2022). However, in the case of the BTB13 core, the initial age model, including magnetostratigraphy and single crystal Ar/Ar sanidine ages for many tuffs in core and outcrop (Deino et al., 2021), was already of very high quality and provided a solid base for establishing a robust astrochronology for the core. Without this initial age control, the significant changes in sedimentation might not have been recognized, leading to an incorrect astronomical tuning. This study therefore demonstrates the importance of an integrated stratigraphic approach in establishing an astronomically-tuned age model (Shanahan et al., 2013; Hilgen et al., 2015; Sinnesael et al., 2019). Astronomical tuning is increasingly used to establish age models both for natural outcrops (Boës et al., 2018) as well as for cores drilled in African lakes (e.g., Lake Bosumtwi; Vinnepand et al., 2024), although some cores that look promising await such attempts (e.g., Lake Chala: Baxter et al., 2024; Lake Malawi; Streib et al., 2024). Such improvements in our age models are critical for resolving the complex climate history of the African continent and its potential connection with global climate change and the evolution and migration of biota, including our ancestors and our own species (see Trauth et al., 2021). This is particularly needed in view of regional differences in climate over the African continent, also in response to astronomical forcing.

6. Conclusions

GD and MS data of the BTB13 core reveals significant variability related to obliquity and precession. Based on initial age control from a Bayesian age model (Deino et al., 2021), it was possible to tune the data to obliquity and subsequently to precession and the 0E1T-1P curve. The final astronomically-tuned age model results in a very good fit between the obliquity- and precession-related variability and the obliquity and precession solutions, respectively. Additionally, amplitude variations of the precession-related variability are consistent with precession-obliquity interference patterns and the 405 kyr eccentricity cycle. Diatomites in the BTB13 region, which concur with GD and MS minima in the core, were interpreted as deep lake phases (Deino et al., 2006). The good fit of our astronomically-tuned age model indicates that the assumed phase relationships are likely correct, suggesting that deep lake phases at the BTB13 site were related to an intensified North African monsoon in response to enhanced boreal summer insolation (i.e., precession minima and obliquity maxima). The formation of diatomites concurred with that of sapropels in the Mediterranean, both in response to wetter conditions on the north(east) African continent. Interestingly, obliquity is dominant throughout the BTB13 records, which is in disagreement with expectations based on low-latitude insolation forcing. Although a low-latitude obliquity signal can be generated by a cross-equatorial insolation gradient (Bosmans et al., 2015b) as well as through the seasonal cycle of equatorial insolation (Berger et al., 2006), in both cases obliquity does not dominate the variability. Possibly, a combination of the two and/or a link to higher latitudes was responsible for the obliquity dominance in the BTB13 records.

CRediT authorship contribution statement

Bianca R. Spiering: Writing – review & editing, Writing – original draft, Visualization, Methodology, Investigation, Formal analysis, Conceptualization. **Mark J. Sier:** Writing – review & editing, Investigation, Funding acquisition. **Frederik J. Hilgen:** Writing – review & editing, Investigation.

Declaration of competing interest

The authors declare that they have no known competing financial interests or personal relationships that could have appeared to influence the work reported in this paper.

Acknowledgements

The authors would like to thank the Hominin Sites and Paleolakes Drilling Project (HSPDP), which was funded by the International

Continental Drilling Program (ICDP) and National Science Foundation (NSF). This work was supported by the Marie Skłodowska-Curie Actions grant to M.J. Sier (Project 101109142, ABCCycle). M.J. Sier is also funded by Social Sciences and Humanities Research Council of Canada (SSHRC) Partnership grant no 895-2024-1005. B.R. Spiering is funded by the Dutch Research Council (NWO; grant number OCENW.M.21.031, awarded to F.J. Hilgen).

Appendix

Table A.1
Obliquity tuning based on correlating the average of GD and MS filtered ~40 kyr (0.02–0.03 1/kyr) cycle minima to obliquity maxima. Bandpass filtering was applied on the data converted to time with the Bayesian age model.

Age filtered cycle minima (ka)	Depth filtered cycle minima (mbs)	Age obliquity maxima (ka)
2582.49453	7.94707124	2588
2623.33288	27.5070408	2627
2665.76968	45.9146526	2670
2707.805455	67.103143	2709
2748.158105	79.4973807	2748
2800.974597	86.9321838	2789
2847.86058	93.3670507	2831
2886.49438	97.289262	2871
2924.882955	102.850124	2911
2961.78968	110.286837	2951
2998.61788	118.357983	2993
3037.84253	129.808378	3038
3079.34123	143.673979	3073
3123.88973	164.517777	3116
3165.506305	177.981263	3159
3206.634255	194.67076	3209
3249.411355	214.580099	3246

Table A.2
Precession tuning based on correlating MS filtered ~20 kyr (0.03–0.07 1/kyr) cycle minima to precession minima. Bandpass filtering was applied on the obliquity-tuned data.

Age filtered cycle minima (ka)	Depth filtered cycle minima (mbs)	Age precession minima (ka)
2590.85508	9.37900144	2591
2608.97076	18.4646976	2613
2635.54276	31.1640596	2636
2655.317	39.6290953	2660
2712.15188	68.1048135	2705
2732.96564	74.7194466	2728
2748.35988	79.5626401	2753
2801.16516	88.7960215	2796
2830.66884	93.3163133	2831
2849.5554	95.1865057	2853
2871.01156	97.2908691	2874
2893.78756	100.457224	2903
2918.409	104.227589	2925
2953.35556	110.739505	2946
2980.82692	116.01868	2968
2998.14836	119.668	2991
3016.91812	124.444026	3017
3037.76692	129.74907	3039
3062.17812	139.386783	3061
3081.74212	147.91163	3083
3108.29076	160.780804	3107
3125.0866	167.362831	3133
3151.72868	175.704581	3154
3173.3834	182.782297	3175
3208.87892	194.630345	3196
3241.45444	212.134178	3250
3256.91876	220.455377	3269

Table A.3
0E1T-1P tuning based on correlating MS filtered ~20 kyr (0.03–0.06 1/kyr) cycle minima to 0E1T-1P maxima. Bandpass filtering was applied on the precession-tuned data.

Age filtered cycle minima (ka)	Depth filtered cycle minima (mbs)	Age 0E1T-1P maxima (ka)
2591.31281	9.50818765	2590
2611.99818	18.0509598	2615
2636.49832	31.339822	2634
2658.77003	39.1952728	2662
2681.83491	53.4460896	2680
2705.99512	68.3910028	2706
2729.36216	74.9833348	2728
2750.67703	79.1126164	2751
2775.69336	84.4355808	2778
2796.88233	88.9099755	2794
2829.86813	93.1701309	2831
2851.82509	95.0866281	2855
2874.88997	97.3880402	2873
2901.85775	100.332508	2905
2924.01615	104.058977	2923
2948.06305	111.23456	2947
2970.59915	116.431077	2967
2992.20359	119.889091	2992
3013.68213	123.834555	3017
3037.65349	129.424375	3039
3061.19679	139.463038	3061
3082.56202	147.741916	3082
3108.45965	161.150322	3108
3131.67561	167.027555	3132
3153.26746	175.413597	3155
3174.31794	182.55242	3174
3197.79829	195.213252	3196
3221.53044	202.905911	3212
3250.57557	212.386253	3249
3269.0451	220.475129	3271

Appendix A. Supplementary data

Supplementary data to this article can be found online at https://doi.org/10.1016/j.palaeo.2025.113377.

Data availability

The authors confirm that all data necessary for supporting the scientific findings of this paper have been provided.

References

Baxter, A.J., Peterse, F., Verschuren, D., Maitituerdi, A., Waldmann, N., Sinninghe Damsté, J.S., 2024. Disentangling influences of climate variability and lake-system evolution on climate proxies derived from isoprenoid and branched glycerol dialkyl glycerol tetraethers (GDGTs): the 250 kyr Lake Chala record. Biogeosciences 21 (11), 2877–2908. https://doi.org/10.5194/bg-21-2877-2024.

Berger, A., Loutre, M.F., Mélice, J.L., 2006. Equatorial insolation: from precession harmonics to eccentricity frequencies. Clim. Past 2, 131–136. https://doi.org/10.5194/cp-2-131-2006.

Boës, X., Prat, S., Arrighi, V., Feibel, C., Haileab, B., Lewis, J., Harmand, S., 2018. Lake-level changes and hominin occupations in the arid Turkana basin during volcanic closure of the Omo River outflows to the Indian Ocean. Quat. Res. 91 (2), 892–909. https://doi.org/10.1017/qua.2018.118.

Bosmans, J.H.C., Drijfhout, S.S., Teunter, E., Hilgen, F.J., Lourens, L.J., 2015a. Response of the North African summer monsoon to precession and obliquity forcings in the EC-Earth GCM. Clim. Dyn. 44, 279–297. https://doi.org/10.1007/s00382-014-2260-z.

Bosmans, J.H.C., Hilgen, F.J., Teunter, E., Lourens, L.J., 2015b. Obliquity forcing of low-latitude climate. Clim. Past 11, 1335–1346. https://doi.org/10.5194/cp-11-1335-2015.

Campisano, C.J., Cohen, A.S., Arrowsmith, J.R., Asrat, A., Behrensmeyer, A.K., Brown, E. T., Deino, A.L., Deocampo, D.M., Feibel, C.S., Kingston, J.D., Lamb, H.F., Lowenstein, T.K., Noren, A., Olago, D.O., Owen, R.B., Pelletier, J.D., Potts, R., Reed, K.E., Renaut, R.W., Russell, J.M., Russell, J.L., Schäbitz, F., Stone, J.R., Trauth, M.H., Wynn, J.G., 2017. The Hominin Sites and Paleolakes Drilling Project: high-resolution paleoclimate records from the East African Rift System and their implications for understanding the environmental context of hominin evolution. PaleoAnthropology 1-43. https://doi.org/10.4207/PA.2017.ART104.

Channell, J.E.T., Singer, B.S., Jicha, B.R., 2020. Timing of Quaternary geomagnetic reversals and excursions in volcanic and sedimentary archives. Quat. Sci. Rev. 228, 106114. https://doi.org/10.1016/j.quascirev.2019.106114.

Chapman, G.R., Brook, M., 1978. Chronostratigraphy of the Baringo Basin, Kenya. Geol. Soc. Lond. Spec. Publ. 6 (1), 207–223.

Cohen, A., Campisano, C., Arrowsmith, R., Asrat, A., Behrensmeyer, A.K., Deino, A., Feibel, C., Hill, A., Johnson, R., Kingston, J., Lamb, H., Lowenstein, T., Noren, A., Olago, D., Owen, R.B., Potts, R., Reed, K., Renaut, R., Schäbitz, F., Tiercelin, J.-J., Trauth, M.H., Wynn, J., Ivory, S., Brady, K., O'Grady, R., Rodysill, J., Githiri, J., Russell, J., Foerster, V., Dommain, R., Rucina, S., Deocampo, D., Russell, J., Billingsley, A., Beck, C., Dorenbeck, G., Dullo, L., Feary, D., Garello, D., Gromig, R., Johnson, T., Junginger, A., Karanja, M., Kimburi, E., Mbuthia, A., McCartney, T., McNulty, E., Muiruri, V., Nambiro, E., Negash, E.W., Njagi, D., Wilson, J.N., Rabideaux, N., Raub, T., Sier, M.J., Smith, P., Urban, J., Warren, M., Yadeta, M., Yost, C., Zinaye, B., 2016. The Hominin Sites and Paleolakes Drilling Project: inferring the environmental context of human evolution from eastern African rift lake deposits. Sci. Drill. 21, 1–16. https://doi.org/10.5194/sd-21-1-2016.

Deino, A.L., Kingston, J.D., Glen, J.M., Edgar, R.K., Hill, A., 2006. Precessional forcing of lacustrine sedimentation in the late Cenozoic Chemeron Basin, Central Kenya Rift, and calibration of the Gauss/Matuyama boundary. Earth Planet. Sci. Lett. 247 (1–2), 41–60. https://doi.org/10.1016/j.epsl.2006.04.009.

Deino, A.L., Sier, M.J., Garello, D.I., Keller, C.B., Kingston, J.D., Scott, J.J., Dupont-Nivet, G., Cohen, A.S., 2021. Chronostratigraphy of the Baringo-Tugen Hills-Barsemoi (HSPDP-BTB13-1A) core – ^{40}Ar/^{39}Ar dating, magnetostratigraphy, tephrostratigraphy, sequence stratigraphy and Bayesian age modeling. Palaeogeogr. Palaeoclimatol. Palaeoecol. 570, 109519. https://doi.org/10.1016/j.palaeo.2019.109519.

Harmand, S., Lewis, J.E., Feibel, C.S., Lepre, C.J., Prat, S., Lenoble, A., Boës, X., Quinn, R. L., Brenet, M., Arroyo, A., Taylor, N., Clément, S., Daver, G., Brugal, J.-P., Leakey, L., Mortlock, R.A., Wright, J.D., Lokorodi, S., Kirwa, C., Kent, D.V., Roche, H., 2015. 3.3-million-year-old stone tools from Lomekwi 3, West Turkana, Kenya. Nature 521, 310–315. https://doi.org/10.1038/nature14464.

Hilgen, F.J., Hinnov, L.A., Aziz, H.A., Abels, H.A., Batenburg, S., Bosmans, J.H.C., De Boer, B., Hüsing, S.K., Kuiper, K.F., Lourens, L.J., Rivera, T., Teunter, E., Van De Wal, R.S.W., Wotzlaw, J.-F., Zeeden, C., 2015. Stratigraphic continuity and fragmentary sedimentation: the success of cyclostratigraphy as part of integrated stratigraphy. Geol. Soc. Lond. Spec. Publ. 404, 157–197. https://doi.org/10.1144/SP404.

Hilgen, F.J., 1991. Extension of the astronomically calibrated (polarity) time scale to the Miocene/Pliocene boundary. Earth Planet. Sci. Lett. 107 (2), 349–368. https://doi.org/10.1016/0012-821X(91)90082-S.
Hilgen, S.L., Hilgen, F.J., Adhityatama, S., Kuiper, K.F., Joordens, J.C.A., 2022. Towards an astronomical age model for the Lower to Middle Pleistocene hominin-bearing succession of the Sangiran Dome area on Java, Indonesia. Quat. Sci. Rev. 297, 107788. https://doi.org/10.1016/j.quascirev.2022.107788.
Husson, D., 2014. MathWorks File Exchange: RedNoise_ConfidenceLevels. https://www.mathworks.com/matlabcentral/fileexchange/45539-rednoise_confidencelevels.
Johnson, T.C., Malala, J.O., 2009. Lake Turkana and its link to the Nile. In: Dumont, H.J. (Ed.), The Nile: Origin, Environments, Limnology and Human Use. Springer Science + Business Media B.V, pp. 287–304.
Joordens, J.C.A., Vonhof, H.B., Feibel, C.S., Lourens, L.J., Dupont-Nivet, G., Van Der Lubbe, J.H.J.L., Sier, M.J., Davies, G.R., Kroon, D., 2011. An astronomically-tuned climate framework for hominins in the Turkana Basin. Earth Planet. Sci. Lett. 307 (1–2), 1–8. https://doi.org/10.1016/j.epsl.2011.05.005.
Kingston, J.D., Deino, A.L., Edgar, R.K., Hill, A., 2007. Astronomically forced climate change in the Kenyan Rift Valley 2.7–2.55 Ma: implications for the evolution of early hominin ecosystems. J. Hum. Evol. 53 (5), 487–503. https://doi.org/10.1016/j.jhevol.2006.12.007.
Kodama, K.P., Hinnov, L.A., 2015. Rock magnetic Cyclostratigraphy. Wiley-Blackwell. https://doi.org/10.1002/9781118561294.
Kuiper, K.F., Deino, A., Hilgen, F.J., Krijgsman, W., Renne, P.R., Wijbrans, J.R., 2008. Synchronizing rock clocks of Earth history. Science 320 (5875), 500–504. https://doi.org/10.1126/science.1154339.
Laskar, J., Robutel, P., Joutel, F., Gastineau, M., Correia, A.C.M., Levrard, B., 2004. A long-term numerical solution for the insolation quantities of the Earth. Astron. Astrophys. 428 (1), 261–285. https://doi.org/10.1051/0004-6361:20041335.
Li, M., Hinnov, L., Kump, L., 2019. Acycle: time-series analysis software for paleoclimate research and education. Comput. Geosci. 127, 12–22. https://doi.org/10.1016/j.cageo.2019.02.011.
Lockwood, C.A., Kimbel, W.H., Johanson, D.C., 2000. Temporal trends and metric variation in the mandibles and dentition of *Australopithecus afarensis*. J. Hum. Evol. 39 (1), 23–55. https://doi.org/10.1006/jhev.2000.0401.
Mantsis, D.F., Lintner, B.R., Broccoli, A.J., Erb, M.P., Clement, A.C., Park, H.-S., 2014. The response of large-scale circulation to obliquity-induced changes in meridional heating gradients. J. Clim. 27 (14), 5504–5516. https://doi.org/10.1175/JCLI-D-13-00526.1.
McClymont, E.L., Ho, S.L., Ford, H.L., Bailey, I., Berke, M.A., Bolton, C.T., De Schepper, S., Grant, G.R., Groeneveld, J., Inglis, G.N., Karas, C., Patterson, M.O., Swann, G.E.A., Thirumalai, K., White, S.M., Alonso-Garcia, M., Anand, P., Hoogakker, B.A.A., Littler, K., Petrick, B.F., Risebrobakken, B., Abell, J.T., Crocker, A.J., De Graaf, F., Feakins, S.J., Hargreaves, J.C., Jones, C.L., Markowska, M., Ratnayake, A.S., Stepanek, C., Tangunan, D., 2023. Climate Evolution Through the Onset and Intensification of Northern Hemisphere Glaciation. Rev. Geophys. 61 (3). https://doi.org/10.1029/2022RG000793 e2022RG000793.
Mitsunaga, B.A., Lupien, R.L., Ouertani, S., Stubbs, B., Deino, A.L., Kingston, J.D., Stockhecke, M., Brown, E.T., Russell, J.M., 2023. High-latitude, Indian Ocean, and orbital influences on Eastern African hydroclimate across the Plio-Pleistocene boundary. Paleoceanograph. Paleoclimatol. 38 (12). https://doi.org/10.1029/2023PA004671 e2023PA004671.
Potts, R., Faith, J.T., 2015. Alternating high and low climate variability: the context of natural selection and speciation in Plio-Pleistocene hominin evolution. J. Hum. Evol. 87, 5–20. https://doi.org/10.1016/j.jhevol.2015.06.014.
Raymo, M.E., 1994. The initiation of northern hemisphere glaciation. Annu. Rev. Earth Planet. Sci. 22, 353–383.
Shanahan, T.M., Peck, J.A., McKay, N., Heil Jr., C.W., King, J., Forman, S.L., Hoffmann, D.L., Richards, D.A., Overpeck, J.T., Scholz, C., 2013. Age models for long lacustrine sediment records using multiple dating approaches – an example from Lake Bosumtwi, Ghana. Quat. Geochronol. 15, 47–60. https://doi.org/10.1016/j.quageo.2012.12.001.
Sier, M.J., Dupont-Nivet, G., Langereis, C., Deino, A.L., Kingston, J.D., Cohen, A.S., 2021. Magnetostratigraphy of the Hominin Sites and Paleolakes Drilling Project (HSPDP) Baringo-Tugen Hills-Barsemoi core (Kenya). Palaeogeogr. Palaeoclimatol. Palaeoecol. 570, 110190. https://doi.org/10.1016/j.palaeo.2020.110190.
Sier, M.J., Spiering, B.R., Dekkers, M.J., Hilgen, F.J., 2025. Magnetic mineralogy of the Baringo core (HSPDP-BTB13-1A, Kenya) shows astronomical forcing with implications for retrieving meaningful paleointensity [version 1]. Open Research Europe 5 (177). https://doi.org/10.12688/openreseurope.20266.1.
Sinnesael, M., De Vleeschouwer, D., Zeeden, C., Batenburg, S.J., Da Silva, A.-C., De Winter, N.J., Dinarès-Turell, J., Drury, A.J., Gambacorta, G., Hilgen, F.J., Hinnov, L. A., Hudson, A.J.L., Kemp, D.B., Lantink, M.L., Laurin, J., Li, M., Liebrand, D., Ma, C., Meyers, S.R., Monkenbusch, J., Montanari, A., Nohl, T., Pälike, H., Pas, D., Ruhl, M., Thibault, N., Vahlenkamp, M., Valero, L., Wouters, S., Wu, H., Claeys, P., 2019. The Cyclostratigraphy Intercomparison Project (CIP): consistency, merits and pitfalls. Earth Sci. Rev. 199, 102965. https://doi.org/10.1016/j.earscirev.2019.102965.
Spiering, B.R., Wubben, E., Hilgen, F.J., Sluijs, A., 2024. Early to Middle Miocene astronomically paced climate dynamics in the Eastern Equatorial Atlantic. Paleoceanograph. Paleoclimatol. 39 (5). https://doi.org/10.1029/2023PA004768 e2023PA004768.
Streib, L.C., Armitage, S.J., Scholz, C.A., 2024. Using luminescence dating to constrain lake sediment records: a new age model for the 1.38 Ma Lake Malawi drill core, Eastern Africa. Quat. Sci. Rev. 334, 108691. https://doi.org/10.1016/j.quascirev.2024.108691.
Thomson, D.J., 1982. Spectrum estimation and harmonic analysis. Proc. IEEE 70 (9), 1055–1096. https://doi.org/10.1109/PROC.1982.12433.
Trauth, M.H., Deino, A.L., Bergner, A.G.N., Strecker, M.R., 2003. East African climate change and orbital forcing during the last 175 kyr BP. Earth Planet. Sci. Lett. 206 (3–4), 297–313. https://doi.org/10.1016/S0012-821X(02)01105-6.
Trauth, M.H., Maslin, M.A., Deino, A.L., Strecker, M.R., Bergner, A.G.N., Dühnforth, M., 2007. High- and low-latitude forcing of Plio-Pleistocene East African climate and human evolution. J. Hum. Evol. 53 (5), 475–486. https://doi.org/10.1016/j.jhevol.2006.12.009.
Trauth, M.H., Asrat, A., Berner, N., Bibi, F., Foerster, V., Grove, M., Kaboth-Bahr, S., Maslin, M.A., Mudelsee, M., Schäbitz, F., 2021. Northern hemisphere glaciation, African climate and human evolution. Quat. Sci. Rev. 268, 107095. https://doi.org/10.1016/j.quascirev.2021.107095.
Verschuren, D., Sinninghe Damsté, J.S., Moernaut, J., Kristen, I., Blaauw, M., Fagot, M., Haug, G.H., CHALLACEA project members, 2009. Half-precessional dynamics of monsoon rainfall near the East African Equator. Nature 462, 637–641. https://doi.org/10.1038/nature08520.
Villmoare, B., Kimbel, W.H., Seyoum, C., Campisano, C.J., Dimaggio, E.N., Rowan, J., Braun, D.R., Arrowsmith, J.R., Reed, K.E., 2015. Early *Homo* at 2.8 Ma from Ledi-Geraru, Afar, Ethiopia. Science 347 (6228), 1352–1355. https://doi.org/10.1126/science.aaa1343.
Vinnepand, M., Zeeden, C., Wonik, T., Gosling, W., Noren, A., Kück, J., Pierdominici, S., Voigt, S., Abadi, M.S., Ulfers, A., Danour, S., Afrifa, K., Kaboth-Bahr, S., 2024. An age-depth model for Lake Bosumtwi (Ghana) to reconstruct one million years of West African climate and environmental change. Quat. Sci. Rev. 325, 108478. https://doi.org/10.1016/j.quascirev.2023.108478.
Westover, K.S., Stone, J.R., Yost, C.L., Scott, J.J., Cohen, A.S., Rabideaux, N.M., Stockhecke, M., Kingston, J.D., 2021. Diatom paleolimnology of late Pliocene Baringo Basin (Kenya) paleolakes. Palaeogeogr. Palaeoclimatol. Palaeoecol. 570, 109382. https://doi.org/10.1016/j.palaeo.2019.109382.